Molecular Cell

Article

Structural basis of TFIIIC-dependent RNA polymerase III transcription initiation

Graphical abstract

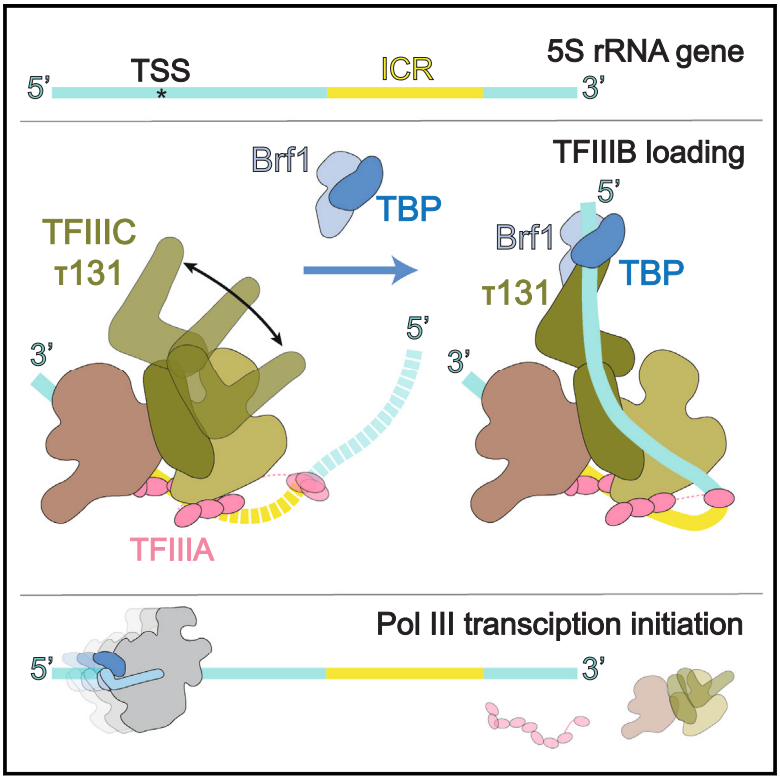

Highlights

- Gene-specific factor TFIIIA acts as an adaptor for TFIIIC-promoter interactions
- The largest subunit τ138 holds together the two lobes of TFIIIC
- τ131 N-terminal domain helps loading Brf1-TBP onto DNA
- Brf1-TBP binding leads to the 5S rRNA gene wrapping around the TFIIIA-TFIIIC body

Authors

Anna Talyzina, Yan Han, Chiranjib Banerjee, Susan Fishbain, Alexis Reyes, Reza Vafabakhsh, Yuan He

Correspondence

yuanhe@northwestern.edu

In brief

Using cryoelectron microscopy and single-molecule FRET experiments, Talyzina et al. elucidated a mechanism by which *S. cerevisiae* transcription factors TFIIIA and TFIIIC recognize 5S rRNA gene promoter and prepare it for RNA polymerase III recruitment. This process involves sharp DNA bending and TFIIIC-assisted loading of TFIIIB upstream of the transcription start site.

Talyzina et al., 2023, Molecular Cell *83*, 2641–2652
August 3, 2023
https://doi.org/10.1016/j.molcel.2023.06.015

CellPress

Molecular Cell

CellPress
OPEN ACCESS

Article

Structural basis of TFIIIC-dependent RNA polymerase III transcription initiation

Anna Talyzina,[1,2] Yan Han,[1,5] Chiranjib Banerjee,[1] Susan Fishbain,[1] Alexis Reyes,[1,2] Reza Vafabakhsh,[1,2] and Yuan He[1,2,3,4,6,*]

[1]Department of Molecular Biosciences, Northwestern University, Evanston, IL, USA
[2]Interdisciplinary Biological Sciences Program, Northwestern University, Evanston, IL, USA
[3]Chemistry of Life Processes Institute, Northwestern University, Evanston, IL, USA
[4]Robert H. Lurie Comprehensive Cancer Center of Northwestern University, Northwestern University, Chicago, IL, USA
[5]Present address: Department of Biophysics, University of Texas Southwestern Medical Center, Dallas, TX, USA
[6]Lead contact
*Correspondence: yuanhe@northwestern.edu
https://doi.org/10.1016/j.molcel.2023.06.015

SUMMARY

RNA polymerase III (Pol III) is responsible for transcribing 5S ribosomal RNA (5S rRNA), tRNAs, and other short non-coding RNAs. Its recruitment to the 5S rRNA promoter requires transcription factors TFIIIA, TFIIIC, and TFIIIB. Here, we use cryoelectron microscopy (cryo-EM) to visualize the *S. cerevisiae* complex of TFIIIA and TFIIIC bound to the promoter. Gene-specific factor TFIIIA interacts with DNA and acts as an adaptor for TFIIIC-promoter interactions. We also visualize DNA binding of TFIIIB subunits, Brf1 and TBP (TATA-box binding protein), which results in the full-length 5S rRNA gene wrapping around the complex. Our smFRET study reveals that the DNA within the complex undergoes both sharp bending and partial dissociation on a slow timescale, consistent with the model predicted from our cryo-EM results. Our findings provide new insights into the transcription initiation complex assembly on the 5S rRNA promoter and allow us to directly compare Pol III and Pol II transcription adaptations.

INTRODUCTION

RNA polymerase III (Pol III) transcribes various types of short, non-coding, and abundant RNAs from three types of promoters. Only type I and II promoters are known in yeast. The type I promoter is found in the 5S ribosomal RNA (rRNA) gene, the type II promoter is associated with transfer RNA (tRNA) genes, and the type III promoter is used in U6 small nuclear RNA (snRNA) genes and others.[1–3] Both type I and type II promoters contain internal control regions (ICRs) in the gene body.[4,5] The ICRs of type I promoter harbor an A-box, an intermediate element (IE), and a C-box, while type II promoter consists of an A-box and a B-box.[6] Generally, Pol III transcription initiation requires transcription factors (TFs), including TFIIIC and TFIIIB.[7] TFIIIA is a specific TF for type I promoters and consists of nine zinc-finger (ZF) repeats in *S. cerevisiae*.[8] TFIIIA was the first gene-specific TF identified in eukaryotes.[4] It also represents the first cloned and sequenced eukaryotic TF, which led to the discovery of ZF motif.[9,10] TFIIIA is the first factor that recognizes and binds the 5S rRNA promoter. The large, six-subunit TFIIIC is recruited to the type I promoter via TFIIIA. In the case of type II promoters, TFIIIC can directly recognize and bind to A-box and B-box elements and recruits TFIIIB, positioning it upstream of the transcription start site (TSS).[11] TFIIIB, which consists of three subunits—TATA-box binding protein (TBP), TFIIB-related factor (Brf1), and B double prime factor (B″)—may support Pol III transcription alone once stably assembled on the promoter, as shown for *S. cerevisiae*.[11] Subunits of TFIIIB only form a stable complex when all of them are bound to DNA.[12] Interestingly, 5S rRNA gene transcription initiation requires both gene-specific (TFIIIA) and general TFs (TFIIIC and TFIIIB).[13] The six subunits of the TFIIIC complex are organized into two lobes: subunits τ131, τ95, and τ55 form the τA lobe, and subunits τ138, τ91, and τ60 form the τB lobe. The two lobes are proposed to be connected via a flexible linker that helps TFIIIC to bind ICRs of different lengths.[14,15] Although several structures of TFIIIC subcomplexes and domains are solved, including the τA lobe,[16] the τ131 N-terminal tetra-trico peptide repeats (TPR) array,[14] the histidine phosphatase domain (HPD) of τ55,[17] the τ138 extended winged-helix (eWH) domain,[14] and a subcomplex of τ60 and τ91,[18] the structure of the complete TFIIIC complex remains elusive, possibly due to its high flexibility. Structures of TFIIIB components have been solved as a part of the Pol III transcription pre-initiation complex (PIC).[19–21] To date, structures of TFIIIA include ZF 1–3 bound to DNA,[22] ZF 4–6 bound to 5S rRNA,[23] and ZF 1–6 bound to 5S rRNA gene.[24] However, the full-length structure of TFIIIA has not been solved.

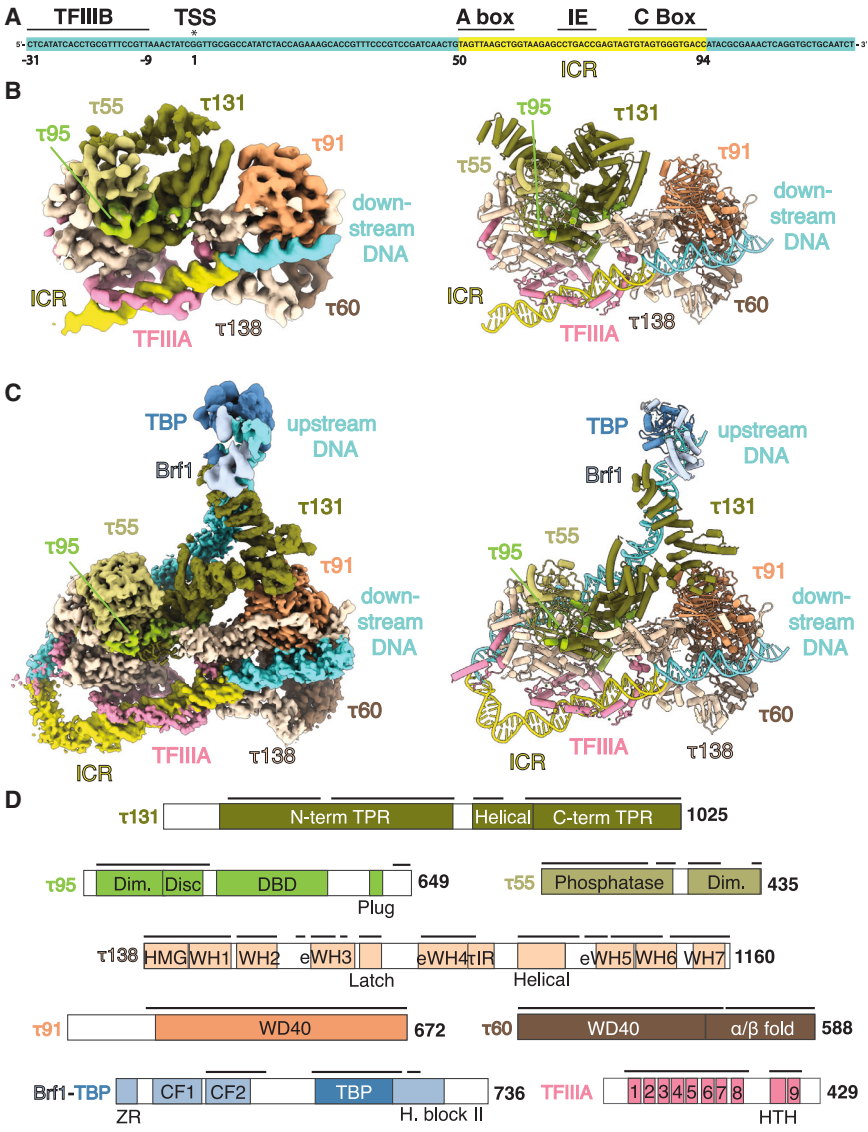

Figure 1. Cryo-EM structures of the TFIIIA-TFIIIC complex and the TFIIIA-TFIIIC-Brf1-TBP complex bound to the 5S rRNA gene

(A) Schematic representation of the DNA template, with transcription start site (TSS) and intermediate element (IE) indicated.

(B) Density map of the TFIIIA-TFIIIC complex (left) and the corresponding model of the TFIIIA-TFIIIC complex (right). The internal control region (ICR) is highlighted.

(C) Composite density map of the TFIIIA-TFIIIC-Brf1-TBP complex (left, see STAR Methods) and the corresponding model of the TFIIIA-TFIIIC-Brf1-TBP complex (right).

(D) Schematic domain representation of TFIIIA, TFIIIC, and Brf1-TBP subunits. The amino-acid lengths of the subunits are labeled at the C termini. Black lines above the bars show the portions for which models were built. Dim., dimerization domains; DBD, DNA-binding domain; HMG, high mobility group box domain; WH, winged helix; eWH, extended winged helix; τIR, τ131-interaction region; ZR, zinc ribbon; CF1,2, cyclin fold 1,2; H. block II, homology block II; TFIIIA 1–9, TFIIIA zinc fingers 1–9; HTH, helix-turn-helix.

See also Figures S1–S4, Tables 1 and 2, and Videos S1 and S2.

Misregulation of Pol III transcription has been linked to cancer,[25–28] with changes in the expression of TFIIIC subunits being associated with infection and disease.[29] Several TFIIIC subunits have been found to be overexpressed in ovarian tumors.[30] Stress conditions have been shown to result in TFIIIC's increased occupancy at tDNAs in yeast and at Alu elements in human cells.[31,32] Additionally, research suggests that human TFIIIC bound to extra TFIIIC (ETC) sites may play a role in chromosome organization, as shown for yeast and humans.[33,34] Despite the importance of these findings, the mechanism by which TFIIIC recruits Pol III to its promoters is not well understood.

Here, we have used cryoelectron microscopy (cryo-EM) to visualize an *S. cerevisiae* complex of TFIIIA and TFIIIC bound to the 5S rRNA gene in the absence of TFIIIB. Additionally, we present a cryo-EM structure of TFIIIA, TFIIIC, and TFIIIB subunits, Brf1 and TBP, bound to the 5S rRNA promoter. We were able to identify all nine TFIIIA ZFs and locate all six subunits of TFIIIC within the complex. Our structure demonstrates how the two largest subunits, τ138 and τ131, hold together the two lobes of TFIIIC. The full-length 5S rRNA gene (151 base pairs [bp] long, including 31 bp upstream the TSS) is wrapped around the TFIIIA-TFIIIC complex. Brf1-TBP binds the upstream region of DNA and contacts the N-terminal region of τ131. We also verify our structural model using single-molecule Förster resonance energy transfer (smFRET) assay, which reveals the dynamic nature of the DNA bound to the complex. We discuss the role of TFIIIC in Pol III PIC assembly and propose a model for how the TFIIIA-TFIIIC complex, bound to ICR, may help TFIIIB in finding its binding site upstream of the TSS.

RESULTS

Assembly of the TFIIIA-TFIIIC complex on promoter DNA facilitates loading of Brf1-TBP

The TFIIIA-TFIIIC and TFIIIA-TFIIIC-Brf1-TBP complexes were assembled on a double-stranded (ds) DNA template composed of the *S. cerevisiae* 5S rRNA gene, including the upstream TFIIIB-binding site and the gene body containing ICR (Figure 1A; see STAR Methods). The complexes were assembled in a stepwise manner using individually purified *S. cerevisiae* factors. Cryo-EM datasets were collected for both complexes, with a subset of 109,548 particles refined to 6.6 Å resolution for the TFIIIA-TFIIIC complex (Figures 1B and S1; Table 1), and a subset of 78,512 particles refined to 3.8 Å resolution for the

Table 1. Cryo-EM data collection, refinement, and validation statistics

	TFIIIA-TFIIIC-Brf1-TBP complex	Focused refinement on the Brf1-TBP-DNA	TFIIIA-TFIIIC complex
PDB code	8FFZ	–	–
EMDB code	29071	29356	29358
Data collection and processing			
Microscope	Titan Krios 3	–	–
Voltage (kV)	300	–	–
Camera	Gatan K3	–	–
Magnification	30k	–	–
Pixel size at detector (Å/pixel)	1.056	1.056	1.079
Total electron exposure (e^{-}/Å^2)	60	60	50
Defocus range (μm)	−2 to −5	−2 to −5	−1.5 to −3
Micrographs used (no.)	23,211	23,211	11,645
Total extracted particles (no.)	5,748,589	5,748,589	2,176,308
Refinement			
Refined particles (no.)	78,512	12,232	109,548
Point-group or helical symmetry parameters	C1	C1	C1
Resolution (global, Å)	3.83	7.14	6.62
FSC threshold	0.143	0.143	0.143
Model composition			
Protein	4,045	–	–
Ligands	9	–	–
RNA/DNA	302	–	–
Model refinement			
Refinement package	Phenix	–	–
-real or reciprocal space	real	–	–
Model-map CC score	0.66	–	–
B factors (Å^2)		–	–
Protein residues	66.73	–	–
Ligands	134.61	–	–
RNA/DNA	193.74	–	–
RMS deviations from ideal values			
Bond lengths (Å)	0.013	–	–
Bond angles (°)	1.971	–	–
Validation			
MolProbity score	1.01	–	–
CaBLAM outliers (%)	1.48	–	–
Clashscore	0.35	–	–
Poor rotamers (%)	0.38	–	–
C-beta deviations	0.44	–	–
Ramachandran plot			
Favored (%)	94.38	–	–
Outliers (%)	0.13	–	–

TFIIIA-TFIIIC-Brf1-TBP complex (Figures 1C and S2; Tables 1 and 2; Videos S1 and S2).

The TFIIIA-TFIIIC and TFIIIA-TFIIIC-Brf1-TBP complexes are assembled on identical DNA templates. The overall conformation of TFIIIC is similar between the two complexes, and the ZF array of TFIIIA interacts with the ICR in a similar manner (Figures 1B, 1C, and S3A). All six subunits of TFIIIC are visible in both complexes (Figures 1B–1D). The two lobes of TFIIIC, τA and τB, are in close contact with each other, held together by multiple interactions with DNA and the τ138 subunit, which is shared between the two lobes. The τA lobe comprises a τ95-τ55 dimer, τ131, and the C-terminal half of τ138. The τB lobe

Table 2. Model-building starting models and model confidence

Subunit/domain	Chain ID	Experimental structures	Alphafold prediction (UniProt ID)	Level of confidence
TFIIIA ZF 1–8	A	PDB: 1TF3 (*Xenopus*)	P39933	atomic level/backbone trace
TFIIIA ZF9	A	–	P39933	rigid body fit
τ138	B	PDB: 5AIM	P34111	atomic level/backbone trace
τ131 N-term TPR	C	PDB: 6YJ6	P33339	rigid body fit
τ131 C-term TPR	C	PDB: 6YJ6	P33339	atomic level/backbone trace
τ95	D	PDB: 6YJ6	P32367	atomic level/backbone trace
τ91	E	PDB: 2J04	Q06339	atomic level/backbone trace
τ60	F	PDB: 2J04	Q12308	atomic level/backbone trace
τ55	G	PDB: 6YJ6	Q12415	atomic level/backbone trace
Brf1-TBP	H	PDB: 6CNB	–	rigid body fit

includes subunits τ91, τ60, and the N-terminal half of τ138. The interaction between τA and TFIIIA, as well as those between τB and DNA, are identical in the two complexes.

The presence of Brf1-TBP in the complex alters the interactions between TFIIIC τA lobe and DNA (Figures 1B and 1C). In the TFIIIA-TFIIIC-Brf1-TBP complex, the DNA upstream of ICR is visible and is stabilized by multiple interactions with TFIIIC τA lobe. The addition of Brf1-TBP dramatically changes the position of τ131 N-terminal TPR array. This part of τ131 is not well resolved in the TFIIIA-TFIIIC complex, possibly due to its unconstrained movement relative to the rest of the complex (Figures S3C and S3D). The residues connecting the N-terminal and C-terminal TPR arrays are not resolved in both structures, suggesting that the two arrays are connected by a flexible "hinge" domain. Interactions between τ131 N-terminal TPR, upstream DNA, and Brf1-TBP lead to the extended conformation of τ131. This state is additionally stabilized by contacts between the "ring" domain of τ131 (residues 390–428) and τ91 (Figures 1B and 1C). TFIIIA ZF 9, bound to the beginning of ICR, becomes visible in this structure. The TFIIIA-TFIIIC-Brf1-TBP complex is resolved to higher resolution; thus, it is used to describe protein-protein interactions within TFIIIC.

τ138 bridges TFIIIC τA and τB lobes

The two largest subunits of TFIIIC, τ138 and τ131, facilitate interactions between the τA and τB lobes (Figures 2A and 2B). This is consistent with previous genetic studies that identified functional connections between τ138 and τ131 in *S. cerevisiae*.[35] These two large subunits also play a role in supporting interactions between subunits within each lobe. TFIIIC is known to accommodate varying lengths of DNA within ICR.[15,36] The observed interactions between the two lobes may contribute to this intriguing ability of TFIIIC.

The domains of τ138, the largest TFIIIC subunit, are distributed between the two lobes (Figure 2A). The N terminus of τ138 belongs to the τB lobe, the middle region is situated in the center, and C terminus is a part of the τA lobe. The compact τA and τB regions of τ138 are connected by a less-structured region (residues 418–739) that contains the eWH4 domain in the middle. Part of this region (residues 641–693) has been shown to be the main link between the two lobes of TFIIIC in *S. cerevisiae*.[14] Subunit τ138 comprises seven WH domains, three of which are eWH (Figures 1D and 2A). The HMG, WH2, and eWH3 domains bind to τ60 subunit, and eWH3 contacts τ91 (Figure S4A), consistent with previous biochemical work in yeast.[18,37] The "latch" domain of τ138 (residues 425–470) is attached to the surface of τ91 WD40 (Figure 2C). The eWH4 domain interacts with the helical domain of τ131 (residues 612–732), and the linker (residues 643–657) connects eWH4 with the τ55-τ95 dimer (Figure S4B). The helical domain of τ138 resides in the τA lobe and interacts with the τ55-τ95 dimer (Figure 2D). eWH5, WH6, and WH7 form a compact structure, interacting with the τ55-τ95 dimer and C-terminal region of τ95 (residues 612–647) (Figure S4C), consistent with previous crosslinking mass spectrometry results.[14] Subunit τ138 serves as a hub that brings together all other parts of the complex by interacting with five other TFIIIC subunits, TFIIIA and DNA (Figures 2A, 3C, and 4B). Additionally, the two largest subunits, τ138 and τ131, also interact with each other (Figure 2E).

τ131 is a component of the τA lobe and is located in the middle of the structure (Figure 2B). The TPRs of τ131 are divided into two modules: N-terminal TPR and C-terminal TPR. The N-terminal TPR is further subdivided into two "arms" with a "ring" domain between them.[14,38] The concave surface of the C-terminal τ131 TPR array accommodates the "disc" domain (residues 161–236) of τ95 (Figure S4D), which is in agreement with previous studies in yeast and humans.[14,16,39] The ring domain of N-terminal TPR also contacts τ91 (residues 259–280) (Figure 2F). Notably, the area of contact between the lobes is smaller in comparison to the area of contact within each lobe (Figures 2C–2F and S4A–S4D). τB lobe has a buried surface area of 6,669 Å^2, while τA lobe buries a large area of 15,828 Å^2. However, the buried surface area between τA and τB is only 675 Å^2.

5S rRNA gene wraps around the complex

The DNA construct used in the experiment is composed of the 5S rRNA gene sequence extended to the upstream TFIIIB-binding region (Figure 1A).[40,41] The TFIIIB-binding sequence (bp −31 to −9) is followed by the TSS (position 1), the ICR (bp 50–94), and the downstream region. The location of Brf1-TBP and TFIIIA are in excellent agreement with the registers of the TFIIIB-binding site and the ICR in the 5S rRNA gene, as determined by tracing the DNA density in the full complex reconstruction. The DNA wraps around the complex and makes multiple contacts with

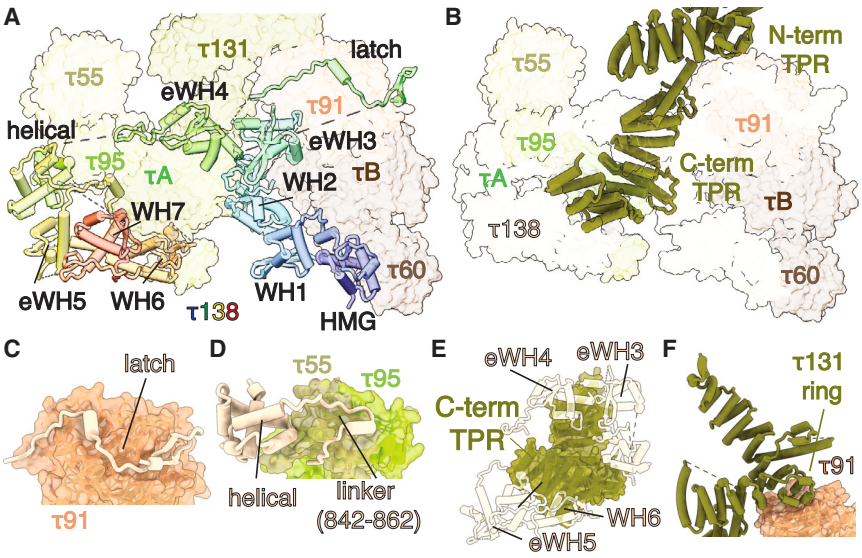

Figure 2. Bridging of TFIIIC τA and τB lobes by the two largest subunits, τ138 and τ131

(A) The τ138 subunit acts as a scaffold for the body of TFIIIC and mediates the interaction between τA and τB lobes. The τ138 subunit is shown as cartoon, while other TFIIIC subunits are shown as transparent surfaces. The τ138 subunit is colored from N terminus to C terminus in a rainbow pattern.

(B) The τ131 subunit is located in the middle of the complex. The C-terminal TPR array of τ131 is buried in the body of the complex, while the N-terminal TPR array is extended away from the body of the TFIIIA-TFIIIC-Brf1-TBP complex. The τ131 subunit is shown as cartoon, with other TFIIIC subunits depicted as transparent surfaces.

(C) The latch of τ138 (residues 425–470) is attached to the surface of τ91.

(D) The helical domain and linker (residues 842–862) of τ138 bind to τ55.

(E) Contacts between τ138 and τ131. The C-terminal TPR of τ131 interacts with eWH4 (residues 1,000–1,023) and WH7 of τ138.

(F) The N-terminal TPR array of τ131 is in the extended state, protruding away from the C-terminal TPR array and the body of TFIIIC. This position is stabilized through interactions of the τ131 ring domain with the τ91 subunit.

See also Figure S4.

TFIIIA, TFIIIC, and Brf1-TBP (Figures 3 and 4A). The path of the bound DNA appears to make a roughly 180° turn, bringing the upstream and downstream regions closer together. The ICR is the most sharply bent region of the DNA (Figure 3A). These findings align with previous research in which both TFIIIA and TFIIIC were shown to introduce bending within DNA in *X. laevis* and *S. cerevisiae*.[42–45] To our knowledge, Pol III system represents the first eukaryotic visualized complex that requires sharp DNA bending in the middle of promoter, which helps one TF (TFIIIC) to position another TF (TFIIIB). Interestingly, similar sharp DNA bending and wrapping is required for transcription initiation in *E. coli*, which was observed in FRET experiments.[46]

The upstream TFIIIB-binding region is recognized by TBP and Brf1.[41,47] The resolution of this part of the map is not sufficient to allow *de novo* model building; hence, the Brf1-TBP-DNA model (PDB: 6cnb) was docked in the map as a rigid body (Figures 3B and S3B). The DNA upstream of the ICR is bound to positively charged patches on the τA lobe, primarily τ131 (residues 192–252; 667–718; 832–841; 924–931) (Figures 3A, S5A, and S5B). The binding of τ131 to the upstream region of the *S. cerevisiae* 5S rRNA and SUP4 tRNA Tyr genes has also been previously shown through site-specific DNA-protein photocrosslinking.[47,48] The first three WH domains of τ138 are wrapped around the DNA downstream of the ICR, following the minor groove of DNA (Figure 3C). The positively charged regions of WH1 and eWH3 have close contacts with the DNA minor and major groove, and similar examples of WH-DNA interactions can be found in other transcription initiation complexes (Figure S4D). The DNA-binding surfaces of τ138 and τ131 have highly conserved residues forming positively charged patches (Figures S5A–S5C, S5E, and S5F). The downstream region of the DNA is bound by the WD40 domain of τ91 subunit (Figures 3D and S5C). This subunit has been shown to photo-crosslink to the very end of the 5S rRNA gene,[47] while the *S. pombe* homolog of τ91, Sfc6p, has been shown to recognize the B-box in type II promoter.[49] This part of the DNA is additionally supported by the τ138 latch (residues 449–470) (Figure 3D).

TFIIIA binds the ICR of the 5S rRNA gene

DNA footprinting assay has revealed that both *X. laevis* and *S. cerevisiae* TFIIIA bind to the ICR of the 5S rRNA gene.[41] DNA binding of the first three ZF in our model is identical to the *X. laevis* TFIIIA-DNA structures but deviates for the following ZF, likely due to the presence of its binding partner, TFIIIC, in the full complex (Figure S6A).[24,41,50] All nine ZFs share the same fold, but ZF 9 has a longer helix (Figure S6B). The ICR is protected by TFIIIA ZF 1–5 and ZF 9, while ZF 6–8 point away from DNA (Figures 3A and 4A). Previous study has shown that purified TFIIIA protects the ICR of the 5S rRNA gene (bp 66–95) from DNase I cleavage, with enhanced cleavage at bp 50 and 65, consistent with our structural model.[41] The footprints of the five N-terminal ZF bound to 5S rRNA gene were indistinguishable from binding of full-length TFIIIA, and it was previously suggested that ZF 6–9 do not bind DNA tightly.[50–52] Consistently, ZF 1–3 in our model bind in the DNA major groove (Figures 4A and S6C).[22,53] ZF 4 traverses the minor groove, while ZF 5 and 9 bind the major groove again (Figures 4A and S6C). The sharpest part of the DNA bend is located between ZF 5 and ZF 9 (Figure 4A). All DNA-binding ZF show positive charge and high conservation of their DNA-contacting surface (Figures 4C, 4D, and S6D).

τ138 was previously suggested to bracket TFIIIA on 5S rRNA gene.[47] Our observation reveals that the contact between TFIIIA and TFIIIC is maintained through τ138, with a large surface area between ZF 6–8 of TFIIIA and residues 980–1,072 of τ138 (Figure 4B). Additionally, ZF 1 and helix-turn-helix domains (residues 331–363) of TFIIIA also contribute to this interaction. This region within the C terminus of *Xenopus* TFIIIA has been identified as a TFIIIC binding and non-DNA-binding site.[54] ZF 7

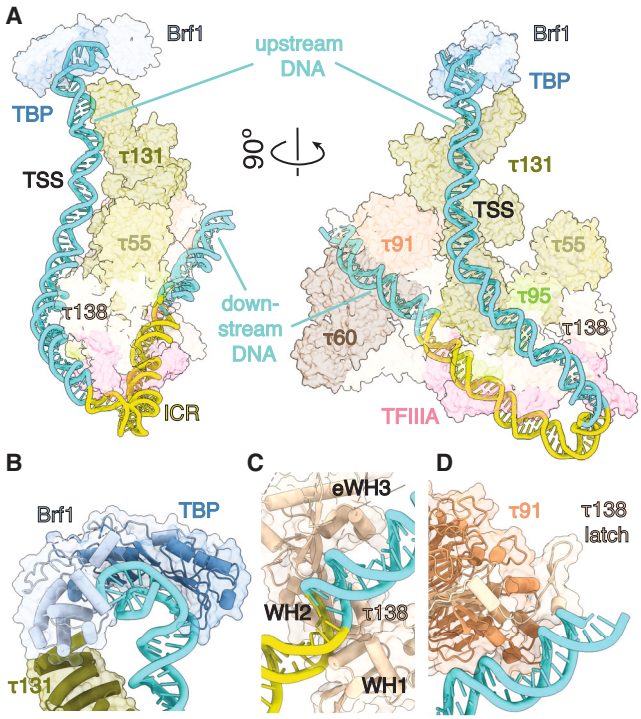

Figure 3. Brf1-TBP binding leads to the 5S rRNA gene wrapping around the TFIIIA-TFIIIC body

(A) DNA wraps around the TFIIIA-TFIIIC-Brf1-TBP complex. The largest protein surfaces that interact with DNA are τ131 and TFIIIA. DNA is shown as cartoon, and proteins are shown as transparent surfaces.

(B) TBP bends upstream DNA region. This part of DNA is stabilized by τ131, TBP, and Brf1.

(C) τ138 WH1, WH2, and eWH3 wrap around downstream DNA.

(D) The end of the 5S rRNA gene is supported by the τB lobe. Both τ91 and the τ138 latch (residues 425–470) are associated with this part of the DNA.

See also Figure S5.

was found to be essential for the assembly of transcriptionally active complex in yeast.[55] The presence of ZF 7–9 has also been shown to be necessary for the transcription activity of the complex, likely due to higher-order interactions in the complex.[51,52] A flexible linker between ZF 8 and 9 is not visible in the map, except for the helix-turn-helix domain (residues 331–363) right next to ZF 9 (Figure 4A). TFIIIA lacking this region (residues 283–364) has been shown to be able to recruit TFIIIC but unable to promote transcription in yeast.[51] Specifically, the deletion of a leucine-rich segment 352-NGLNLLLN-359, a small helix next to ZF 9, resulted in the loss of transcription activity in *S. cerevisiae*.[56] This helix appears to be an anchor point of ZF 9 on the surface of τ138 (Figure 4B).

smFRET shows the dynamic nature of the complex

To understand the conformational dynamics of the complex and independently verify our structural model, we perform smFRET assay using the full TFIIIA-TFIIIC-Brf1-TBP complex (Figure 5A). We purified the complex using a dsDNA molecule labeled with Cy3 and Cy5, following the same protocol as for the cryo-EM sample preparation (see STAR Methods). The positions of Cy3 and Cy5 were chosen such that, based on our structure, they are 66 Å apart in the assembled complex, which would allow for efficient FRET (Figure 3A). The DNA-only sample shows stable FRET close to zero, indicating an extended conformation of the DNA (Figures 5B and S7A). The TFIIIA-TFIIIC-Brf1-TBP complex assembled on the DNA shows two higher FRET states (Figures 5C and S7B). The FRET histogram shifts to higher FRET, indicating a decrease in the distance between the fluorophores (Figure 5D). Notably, most traces (62%) display slow transitions between the two FRET states at 0.07 and 0.22 before photobleaching (Figures 5C, 5E, and S7B). The second FRET peak for the full complex at a FRET value of 0.22 corresponds to a generic distance of 66 Å, which is consistent with our prediction from the structure, confirming that this is the wrapped DNA conformation. To further investigate the nature of the low FRET state, we conduct the experiment on the complex that is assembled without Brf1-TBP (Figure S7C). The FRET histogram for this complex shows a single major peak at a FRET value of 0.07, similar to the lower FRET peak for the full complex, suggesting that this represents a dynamic, partially unwrapped intermediate (Figure 5D). The presence of this lower FRET state in TFIIIA-TFIIIC-Brf1-TBP complex trajectories suggests that this complex is dynamic and the upstream DNA is not always bound by both TFIIIC and Brf1-TBP. We performed the experiment with the DNA and TFIIIA only (Figures S7D and S7E). Interestingly, we observed a small percentage of DNA molecules showing very brief and infrequent visits to a higher FRET state, consistent with the possibility that TFIIIA alone can induce transient bending of DNA. The frequency and lifetime of these bent states were much shorter than what we observed in the presence of all the three proteins, suggesting that TFIIIC and Brf1-TBP are essential for supporting the bent DNA.

DISCUSSION

Historically, biochemical studies of Pol III transcription machinery have shaped our understanding of eukaryotic transcription. However, structural basis of TFIIIC-dependent Pol III promoter recruitment remained elusive. In this study, we have visualized TFIIIA-TFIIIC and TFIIIA-TFIIIC-Brf1-TBP complexes assembled on 5S rRNA gene. The overall conformation of TFIIIC in both complexes is similar, but the N-terminal TPR of τ131 is poorly resolved in the TFIIIA-TFIIIC complex. This part of τ131 is stabilized by interactions with Brf1-TBP and upstream DNA in our second structure. The largest TFIIIC subunit τ138 links the two lobes of TFIIIC and interacts with the other five TFIIIC subunits, TFIIIA, and DNA. TFIIIA ZF 1–5 and 9 are bound to the ICR of 5S rRNA gene, while ZF 6–8 interacts with τ138, representing a major contact between TFIIIA and TFIIIC. The DNA makes a 180° turn within the TFIIIA-TFIIIC-Brf1-TBP complex. We used smFRET to investigate the conformational dynamics of the DNA within TFIIIA-TFIIIC-Brf1-TBP complex. The DNA-only control exhibited stable FRET close to zero, while the TFIIIA-TFIIIC-Brf1-TBP complex assembled on the DNA showed two higher FRET states at 0.07 and 0.22, with the latter corresponding to a 66 Å distance of the two fluorophores, consistent with our cryo-EM structure. The FRET value of 0.07 was also observed in the TFIIIA-TFIIIC-DNA complex, indicating a partially unwrapped intermediate.

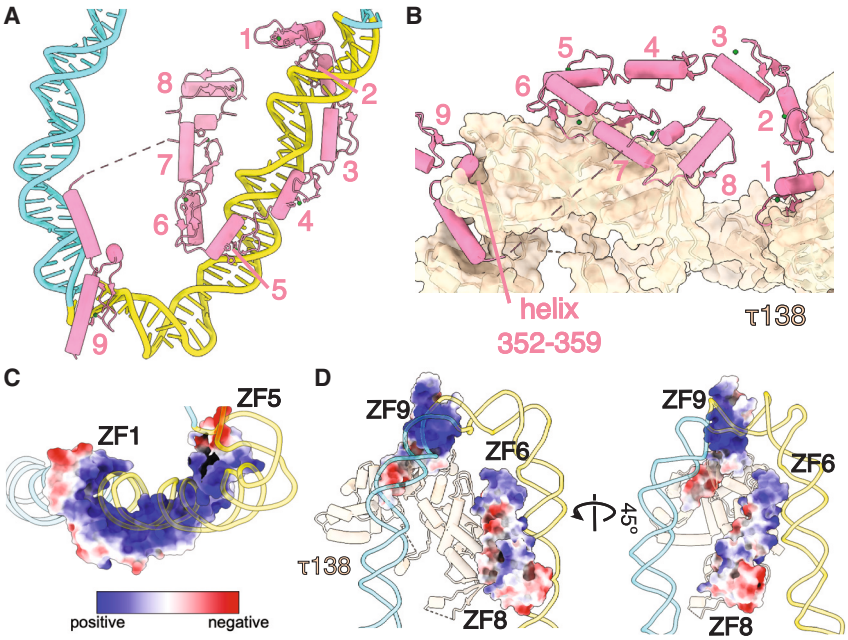

Figure 4. TFIIIA binds the ICR of the 5S rRNA gene

(A) ZF 1–5 and ZF 9 bind DNA in the ICR, while ZF 6–8 protrude away from ICR. The most sharply bent region of DNA is located between ZF 5 and 9.

(B) TFIIIA has a large interaction surface with τ138. ZF 1, 6–8, and a helix near ZF 9 contribute to the interaction.

(C) DNA-binding residues of ZF 1–5 form a large, extended, positively charged surface. TFIIIA is shown as surface and colored according to Coulombic potential. The model is colored in a range from red for negative potential to blue for positive potential.

(D) ZF 6–8 do not interact with DNA as closely as the first five ZFs, but their positively charged surfaces are directed toward DNA and away from τ138. ZF 9 DNA-binding surface is positively charged. TFIIIA is shown as surface and colored according to Coulombic potential. The model is colored in a range from red for negative potential to blue for positive potential.

See also Figure S6.

Based on the cryo-EM structures and smFRET data, we propose a model for the TFIIIA-TFIIIC-mediated assembly of the Pol III PIC. Before the complex assembles, the two lobes of TFIIIC, connected by the τ138 linker, may move relative to each other (Figure 6, state 1). This relative flexibility of the lobes has been previously observed by EM in yeast.[15] We also observe different positions of the TFIIIC lobes by negative stain EM (Figure S8A). The assembly of the Pol III PIC is thought to begin with TFIIIA locating the 5S rRNA gene,[41,57,58] likely introducing initial bending that is mostly localized within the ICR.[43,44] In our structure, only ZF 1–5 and ZF 9 are bound to DNA. However, when TFIIIA first binds DNA, all nine ZF may make DNA contacts, similar to *X. laevis* TFIIIA.[59,60] In our structure, ZF 1–5 bind 29 bp, while ZF 9 protects 5 bp of the ICR. This leaves about one turn of DNA (11 bp) that, in principle, can be occupied by ZF 6–8 in this initial phase. The binding of ZF 6–8 may be similar to the DNA-binding mode of ZF 1–3. Compared with the first five ZF, ZF 6–8 have smaller positively charged areas, which may make them easier to be peeled off from DNA when the TFIIIA-TFIIIC complex forms (Figures 4C and 4D). Alternatively, ZF 6–8 may be in search of TFIIIC instead of binding to DNA. This first "searching" state can be characterized by the flexibility of the TFIIIA-DNA complex and within the unrestrained TFIIIC.

Once TFIIIC binds TFIIIA and downstream DNA, the mobility between the τA and τB lobes becomes limited (Figure 6, state 2). The ICR and downstream DNA is fixed via interactions with ZF 1–5 of TFIIIA and τB lobe. The upstream DNA may still move due to the presence of a flexible linker within TFIIIA. This movement of upstream DNA can assist in the search for τ131 and/or Brf1-TBP binding. The lower FRET state of 0.07 may correspond to this complex (Figure 5D). The C-terminal TPR array of τ131 is locked in the body of the complex, while the N-terminal TPR array is not restrained. The hinge region between the N-terminal and C-terminal TPRs allows for the potential movement of the N-terminal TPR array from the closed state, where it contacts the C-terminal TPR,[16] to the fully open state, where it is rotated by approximately 180° relative to its position in the closed state (Figure S3D). In this "ruling" phase, the conformational sampling of the τ131 N terminus may help to search for Brf1-TBP and DNA. The variable distance between the N-terminal and C-terminal TPR arrays of τ131 can act as a ruler: simultaneous interactions of τ131 with TFIIIB and the TFIIIB-binding region of DNA are possible only when τ131 N terminus is located within a certain distance from the C-terminal TPR (Video S2). We propose this model of TFIIIC-aided TFIIIB recruitment as an extension of the previously communicated models.[16,61–63]

The TFIIIA-TFIIIC-Brf1-TBP complex, which we observe after adding Brf1-TBP to TFIIIA-TFIIIC complex, corresponds to the "locking" state (Figure 6, state 3). In this state, the N-terminal TPR array of τ131 is fixed in the open conformation. This position of τ131 opens a positively charged patch on its surface (Figures S5A–S5C). Yeast two-hybrid assays have shown that Brf1 interacts with the N terminus of τ131 subunit, and this result has been supported by mutagenesis analysis and binding assays.[38,64–67] The sharpest bend in DNA is located between TFIIIA ZF 5 and 9 within the ICR region. This bent DNA is stabilized through interactions with TFIIIA and τ131 (Figures 3A, 4A, and S5A–S5C). Upstream DNA is bound by TBP, Brf1, and the N terminus of τ131. In the smFRET assay, this state is represented by the 0.22 FRET efficiency state (Figure 5D). DNAse I footprinting has shown that TFIIIA protects the ICR of the 5S rRNA gene, and the binding of TFIIIC to TFIIIA-DNA can extend the footprint in two ways: a "core" footprint on the downstream DNA or "extended" footprint up to upstream DNA region bp −20.[41] The addition of TFIIIB extends DNA protection up to bp −45, and the TFIIIA-TFIIIC-TFIIIB complex protects the DNA from bp −45 to 120.[41] Similar footprinting patterns have been observed for tRNA genes as well.[68]

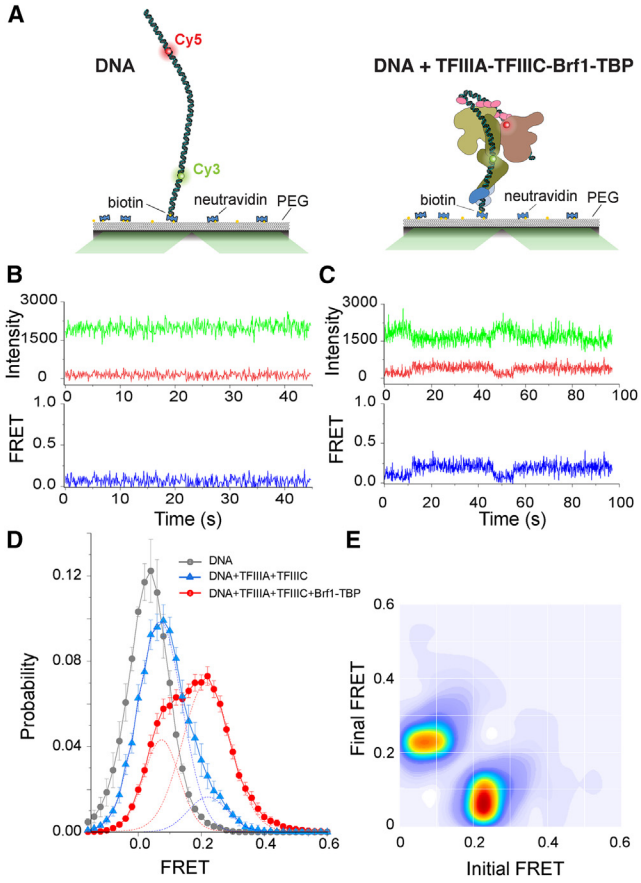

Figure 5. smFRET reveals DNA bending that is consistent with the cryo-EM study

(A) Schematic representation of the smFRET assay. Left, labeled DNA; right, labeled DNA + TFIIIA-TFIIIC-Brf1-TBP complex.

(B) Representative single-molecule time traces of DNA-only sample showing donor (green) and acceptor (red) intensities and the corresponding FRET (blue).

(C) Representative single-molecule time traces of the TFIIIA-TFIIIC-Brf1-TBP complex showing donor (green) and acceptor (red) intensities and the corresponding FRET (blue). The FRET data show the presence of two states.

(D) smFRET population histogram of DNA only, DNA + TFIIIA-TFIIIC, and DNA + TFIIIA-TFIIIC-Brf1-TBP. Data represents mean ± SEM. The histogram of DNA + TFIIIA-TFIIIC is fitted to two Gaussian distributions (blue dashed line) centered on 0.07 and 0.22, respectively. The histogram of the full complex, DNA + TFIIIA-TFIIIC-Brf1-TBP, is also fitted to two Gaussian distributions (red dashed line) centered on 0.07 and 0.22, respectively.

(E) Transition density plot of the full complex, DNA + TFIIIA-TFIIIC-Brf1-TBP. Transitions are from two independent measurements.

See also Figure S7.

The TFIIIA-TFIIIC-Brf1-TBP state that we capture in this study is not compatible with Pol III binding. Alignment of Brf1-TBP from Pol III PIC structures with Brf1-TBP in our model results in severe clashes between Pol III and TFIIIC (Figure S8D). Therefore, it is suggested that direct interaction between Pol III and TFIIIC may be not necessary for Pol III recruitment to promoter. Previous study has shown that once TFIIIB is assembled on DNA, TFIIIC is dispensable for in vitro transcription.[11] Additionally, yeast TFIIIC and Pol III occupancy on DNA is inversely correlated, as shown by chromatin immunoprecipitation.[31] The interaction between Brf1, B″, and τ131 also increases during transcription repression.[31] Furthermore, smFRET data demonstrate that the DNA within the TFIIIA-TFIIIC-Brf1-TBP complex is not static and undergoes spontaneous transitions on slow timescales (10 s of seconds) to a partially unwrapped state (Figure 5C). This state could be crucial for allowing Pol III to bind productively.

Finally, the TFIIIC complex needs to be displaced from DNA to allow Pol III transcription. The B″ binding and completion of TFIIIB may trigger a transition to a new state where the contact between τ131 and Brf1-TBP is broken, resulting in the detachment of TFIIIC τA lobe from DNA (Figure 6, state 4). At the same time, the stable TFIIIB-DNA complex is assembled and can recruit Pol III.[11,58] This "Pol III loading" state may resemble yeast and human Pol III PIC structures.[19–21] Once the PIC is formed, Pol III may initiate transcription. For transcription to occur over the full length of the gene, both TFIIIC and TFIIIA need to be displaced from the DNA.

TFIIIC in Pol III system and TFIID in Pol II system play similar roles in transcription initiation (Figure S8). TFIIIC and TFIID are large protein complexes with multiple lobes. TFIIIC is split into two lobes τA and τB, while TFIID has three lobes: A, B, and C (Figures S8B and S8E). Both TFIIIC and TFIID extensively bind promoter DNA in the intragenic regions using several binding surfaces (Figures S8B, S8C, and S8F). Both factors can position TBP near its DNA-binding site (Figures S8C and S8F). This TBP positioning requires a large structural rearrangement of τ131 N-terminal TPR in TFIIIC (Figure S8, compare B and C). Similarly, lobe A moves relative to the rest of TFIID to load TBP on DNA (Figure S8, compare E and F). However, PIC assembly will likely look different between Pol III and Pol II. Superposition of the Pol III PIC on TFIIIA-TFIIIC-Brf1-TBP showed severe clashes between Pol III and TFIIIC (Figure S8D). This suggests that TFIIIC must be displaced from promoter to allow Pol III transcription initiation. TFIID, on the contrary, can accommodate Pol II PIC assembly with minimal rearrangements (Figure S8G). This difference between TFIIIC-assisted and TFIID-assisted PIC assembly may reflect functional differences between Pol III and Pol II. Although Pol III is recognized for its fast and high-throughput transcription, the initiation of Pol II transcription requires precise control.

Finally, we would like to discuss the role of the TFIIIA-TFIIIC complex in the context of chromatin. The 5S rRNA gene contains a strong nucleosome positioning sequence, and the nucleosome dyad position overlaps with TSS.[69,70] Untimely 5S nucleosome assembly can impede transcription initiation by Pol III. The TFIIIA-TFIIIC complex may play an important role in displacing the nucleosome, allowing for the formation of the transcription initiation complex. Once the nucleosome is removed and TFIIIA-TFIIIC is bound to the promoter region, TFIIIC assists in assembling TFIIIB. In contrast to the 5S nucleosome, DNA-bound TFIIIC enables TFIIIB and Pol III to access the DNA and initiate transcription promptly. We suggest that the DNA is wrapped around the TFIIIA-TFIIIC complex to ensure fast access to the promoter region and protect the DNA from 5S nucleosome reassembly. Therefore, the sharp bending of DNA and the extensive contact between TFIIIA-TFIIIC and DNA in our structure can serve two purposes simultaneously: guiding TBP toward its binding sequence and preventing the reassembly of the 5S nucleosome.

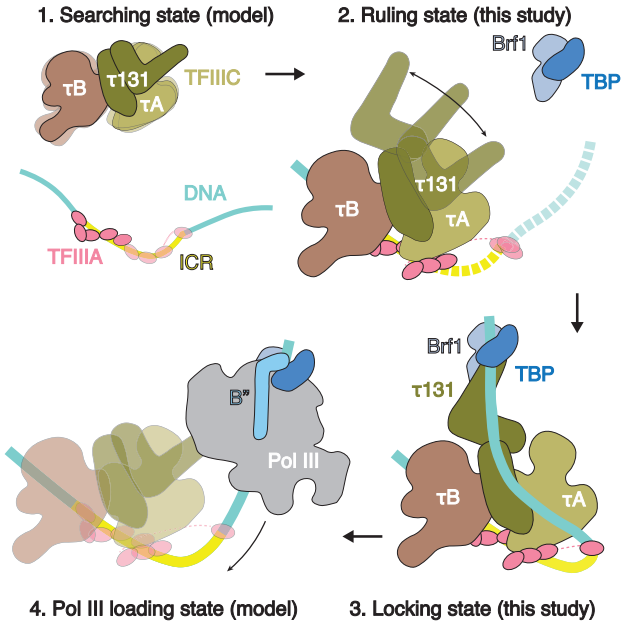

Figure 6. Model of TFIIIC-dependent Pol III PIC assembly on 5S rRNA gene

(1) Searching state (model): the two lobes of TFIIIC are not restrained by DNA binding and may move relative to each other. TFIIIA recognizes the ICR of the 5S rRNA gene. ZF 6–9 are shown as semi-transparent cartoons to reflect the uncertainty in their position.

(2) Ruling state (formation of the TFIIIA-TFIIIC-DNA complex, visualized in this study): TFIIIC binds TFIIIA and DNA downstream of ICR. These interactions restrain mobility between the τA and τB lobes of TFIIIC. The "hinge" region between the N-terminal TPR and C-terminal TPR of τ131 allows the N-terminal TPR (shown as semi-transparent surface) to transition from the closed state (N-terminal TPR contacts C-terminal TPR) to the fully open state (N-terminal TPR array is turned by 180° relative to its position in the closed state). This sampling movement may help τ131 N-terminal TPR to search for Brf1 and/or DNA for binding. The ICR and downstream DNA is fixed via interactions with ZF 1–5 of TFIIIA and the τB lobe. The flexibility within the upstream DNA helps to search for τ131 and/or Brf1 binding. This complex may represent the "ruling" state of τ131 because the distance between the N-terminal and C-terminal TPRs of τ131 is variable, but strong τ131-DNA interaction is only possible when N-terminal TPR is in the extended conformation. This allows τ131 to measure the distance from ICR to the TFIIIB-binding region. Upstream DNA, not visible in the structure, is depicted as a dashede line.

(3) Locking state (formation of the TFIIIA-TFIIIC-Brf1-TBP-DNA complex, visualized in this study): N-terminal TPR array of τ131 is in the extended state. DNA is bent within the ICR, and upstream DNA is bound to the surface of the τA lobe. DNA upstream of TSS is bound by TBP, Brf1, and the N terminus of τ131.

(4) Pol III loading state (model): once Brf1 and TBP locate the TFIIIB-binding site and bind it, B″ and Pol III can be recruited. Pol III may then initiate transcription, while TFIIIC and TFIIIA (both shown as semi-transparent surfaces) have to be displaced from DNA to allow Pol III to transcribe the full length of the gene.

See also Figure S8.

Limitations of the study

Our studies provide a basis to understand how TFIIIA-TFIIIC complex guides TBP toward its DNA-binding site and therefore prepares the promoter for TFIIIB loading, followed by Pol III recruitment. However, Brf1-TBP fusion protein is used instead of the two separate factors. This fusion protein was shown to effectively replace Brf1 and TBP in TFIIIC-dependent transcription.[71] Nevertheless, future studies are necessary to investigate the details of the three separate TFIIIB subunits interacting with DNA and TFIIIC in the context of Pol III promoter recruitment. Moreover, the ICR within 5S rRNA promoter (type I) is different from tRNA promoters (type II). Furthermore, tRNA promoters have variable distances between the elements of ICR. Hence, structural studies of TFIIIC interactions with different tRNA promoters can potentially explain how a single TFIIIC factor may accommodate both type I and type II Pol III promoters.

STAR★METHODS

Detailed methods are provided in the online version of this paper and include the following:

- KEY RESOURCES TABLE
- RESOURCE AVAILABILITY
  - Lead contact
  - Materials availability
  - Data and code availability
- EXPERIMENTAL MODEL AND STUDY PARTICIPANT DETAILS
- METHOD DETAILS
  - Purification of TFIIIA
  - Purification of TFIIIC
  - Purification of Brf1-TBP
  - Complex assembly
  - Negative stain EM data collection and processing
  - Cryo-EM sample preparation
  - Cryo-EM data collection and processing
  - Model building and refinement
  - Preparation of DNA constructs for smFRET
  - Complex assembly and pulldown for smFRET
  - smFRET measurements
  - smFRET data analysis
- QUANTIFICATION AND STATISTICAL ANALYSIS

SUPPLEMENTAL INFORMATION

Supplemental information can be found online at https://doi.org/10.1016/j.molcel.2023.06.015.

ACKNOWLEDGMENTS

We thank past and present lab members for advice, assistance, and comments on the manuscript. We thank Jason Pattie for computer support. We thank Janette Meyers, Rose Marie Haynes, and Harry Scott at the PNCC for data collection support. We thank the staff at the Structural Biology Facility (SBF) of Northwestern University for technical support. Y. He was supported by an Institutional Research Grant from the American Cancer Society (IRG-15-173-21), NIGMS (R01GM135651 and R01GM144559), NCI (P01CA092584), and an H Foundation Core Facility Pilot Project Award. R.V. was supported by NIGMS (R01GM140272) and The Searle Leadership Fund for the Life Sciences at Northwestern University. R.V. was supported by the National Institutes of Health grant R01GM140272. Y. He and R.V. were supported by Chicago Biomedical Consortium with support from the Searle Funds at The Chicago Community Trust. A.T. and A.R. were supported by NIGMS (5T32GM140995). A portion of this research was supported by NIH grant U24GM129547 and performed at the PNCC at OHSU and accessed through EMSL (grid.436923.9), a DOE Office of Science User Facility sponsored by

the Office of Biological and Environmental Research. This work used resources of the Northwestern University Structural Biology Facility, which is generously supported by the NCI CCSG P30 CA060553 grant awarded to the Robert H. Lurie Comprehensive Cancer Center. We acknowledge the use of the Ametek K3 direct electron detector, which was generously provided by Professor Robert A. Lamb, Ph.D., Sc.D., HHMI investigator.

AUTHOR CONTRIBUTIONS

Y. He, Y. Han, and A.T. conceived the project. Y. Han, S.F., A.R., and A.T. purified proteins. A.T. and Y. Han assembled the complexes and prepared cryo-EM samples. A.T. and Y. Han processed cryo-EM data. A.T. built atomic models. C.B. and R.V. collected and processed single molecule data. A.T. and Y. He wrote the manuscript with input from all authors.

DECLARATION OF INTERESTS

The authors declare no competing interests.

INCLUSION AND DIVERSITY

We support inclusive, diverse, and equitable conduct of research.

Received: February 6, 2023
Revised: May 2, 2023
Accepted: June 8, 2023
Published: July 3, 2023

REFERENCES

1. Dieci, G., Fiorino, G., Castelnuovo, M., Teichmann, M., and Pagano, A. (2007). The expanding RNA polymerase III transcriptome. Trends Genet. *23*, 614–622. https://doi.org/10.1016/j.tig.2007.09.001.
2. Arimbasseri, A.G., and Maraia, R.J. (2016). RNA polymerase III advances: structural and tRNA functional views. Trends Biochem. Sci. *41*, 546–559. https://doi.org/10.1016/j.tibs.2016.03.003.
3. Wang, Q., Daiß, J.L., Xu, Y., and Engel, C. (2022). Snapshots of RNA polymerase III in action - a mini review. Gene *821*, 146282. https://doi.org/10.1016/j.gene.2022.146282.
4. Engelke, D.R., Ng, S.Y., Shastry, B.S., and Roeder, R.G. (1980). Specific interaction of a purified transcription factor with an internal control region of 5S RNA genes. Cell *19*, 717–728. https://doi.org/10.1016/s0092-8674(80)80048-1.
5. Guffanti, E., Ferrari, R., Preti, M., Forloni, M., Harismendy, O., Lefebvre, O., and Dieci, G. (2006). A minimal promoter for TFIIIC-dependent in vitro transcription of SnoRNA and tRNA genes by RNA polymerase III. J. Biol. Chem. *281*, 23945–23957. https://doi.org/10.1074/jbc.M513814200.
6. Geiduschek, E.P., and Tocchini-Valentini, G.P. (1988). Transcription by RNA polymerase III. Annu. Rev. Biochem. *57*, 873–914. https://doi.org/10.1146/annurev.bi.57.070188.004301.
7. Ferrari, R., Rivetti, C., Acker, J., and Dieci, G. (2004). Distinct roles of transcription factors TFIIIB and TFIIIC in RNA polymerase III transcription reinitiation. Proc. Natl. Acad. Sci. USA *101*, 13442–13447. https://doi.org/10.1073/pnas.0403851101.
8. Camier, S., Dechampesme, A.M., and Sentenac, A. (1995). The only essential function of TFIIIA in yeast is the transcription of 5S rRNA genes. Proc. Natl. Acad. Sci. USA *92*, 9338–9342. https://doi.org/10.1073/pnas.92.20.9338.
9. Ginsberg, A.M., King, B.O., and Roeder, R.G. (1984). Xenopus 5S gene transcription factor, TFIIIA: characterization of a cDNA clone and measurement of RNA levels throughout development. Cell *39*, 479–489. https://doi.org/10.1016/0092-8674(84)90455-0.
10. Miller, J., McLachlan, A.D., and Klug, A. (1985). Repetitive zinc-binding domains in the protein transcription factor IIIA from Xenopus oocytes. EMBO J. *4*, 1609–1614. https://doi.org/10.1002/j.1460-2075.1985.tb03825.x.
11. Kassavetis, G.A., Braun, B.R., Nguyen, L.H., and Peter Geiduschek, E.P. (1990). S. cerevisiae TFIIIB is the transcription initiation factor proper of RNA polymerase III, while TFIIIA and TFIIIC are assembly factors. Cell *60*, 235–245. https://doi.org/10.1016/0092-8674(90)90739-2.
12. Cloutier, T.E., Librizzi, M.D., Mollah, A.K., Brenowitz, M., and Willis, I.M. (2001). Kinetic trapping of DNA by transcription factor IIIB. Proc. Natl. Acad. Sci. USA *98*, 9581–9586. https://doi.org/10.1073/pnas.161292298.
13. Lassar, A.B., Martin, P.L., and Roeder, R.G. (1983). Transcription of class III genes: formation of preinitiation complexes. Science *222*, 740–748. https://doi.org/10.1126/science.6356356.
14. Male, G., von Appen, A., Glatt, S., Taylor, N.M., Cristovao, M., Groetsch, H., Beck, M., and Müller, C.W. (2015). Architecture of TFIIIC and its role in RNA polymerase III pre-initiation complex assembly. Nat. Commun. *6*, 7387. https://doi.org/10.1038/ncomms8387.
15. Schultz, P., Marzouki, N., Marck, C., Ruet, A., Oudet, P., and Sentenac, A. (1989). The two DNA-binding domains of yeast transcription factor tau as observed by scanning transmission electron microscopy. EMBO J. *8*, 3815–3824.
16. Vorländer, M.K., Jungblut, A., Karius, K., Baudin, F., Grötsch, H., Kosinski, J., and Müller, C.W. (2020). Structure of the TFIIIC subcomplex tauA provides insights into RNA polymerase III pre-initiation complex formation. Nat. Commun. *11*, 4905. https://doi.org/10.1038/s41467-020-18707-y.
17. Taylor, N.M., Glatt, S., Hennrich, M.L., von Scheven, G., Grötsch, H., Fernández-Tornero, C., Rybin, V., Gavin, A.C., Kolb, P., and Müller, C.W. (2013). Structural and functional characterization of a phosphatase domain within yeast general transcription factor IIIC. J. Biol. Chem. *288*, 15110–15120. https://doi.org/10.1074/jbc.M112.427856.
18. Mylona, A., Fernández-Tornero, C., Legrand, P., Haupt, M., Sentenac, A., Acker, J., and Müller, C.W. (2006). Structure of the tau60/Delta tau91 subcomplex of yeast transcription factor IIIC: insights into preinitiation complex assembly. Mol. Cell *24*, 221–232. https://doi.org/10.1016/j.molcel.2006.08.013.
19. Han, Y., Yan, C., Fishbain, S., Ivanov, I., and He, Y. (2018). Structural visualization of RNA polymerase III transcription machineries. Cell Discov. *4*, 40. https://doi.org/10.1038/s41421-018-0044-z.
20. Abascal-Palacios, G., Ramsay, E.P., Beuron, F., Morris, E., and Vannini, A. (2018). Structural basis of RNA polymerase III transcription initiation. Nature *553*, 301–306. https://doi.org/10.1038/nature25441.
21. Vorländer, M.K., Khatter, H., Wetzel, R., Hagen, W.J.H., and Müller, C.W. (2018). Molecular mechanism of promoter opening by RNA polymerase III. Nature *553*, 295–300. https://doi.org/10.1038/nature25440.
22. Foster, M.P., Wuttke, D.S., Radhakrishnan, I., Case, D.A., Gottesfeld, J.M., and Wright, P.E. (1997). Domain packing and dynamics in the DNA complex of the N-terminal zinc fingers of TFIIIA. Nat. Struct. Biol. *4*, 605–608. https://doi.org/10.1038/nsb0897-605.
23. Lee, B.M., Xu, J., Clarkson, B.K., Martinez-Yamout, M.A., Dyson, H.J., Case, D.A., Gottesfeld, J.M., and Wright, P.E. (2006). Induced fit and "lock and key" recognition of 5S RNA by zinc fingers of transcription factor IIIA. J. Mol. Biol. *357*, 275–291. https://doi.org/10.1016/j.jmb.2005.12.010.
24. Nolte, R.T., Conlin, R.M., Harrison, S.C., and Brown, R.S. (1998). Differing roles for zinc fingers in DNA recognition: structure of a six-finger transcription factor IIIA complex. Proc. Natl. Acad. Sci. USA *95*, 2938–2943. https://doi.org/10.1073/pnas.95.6.2938.
25. White, R.J. (2004). RNA polymerase III transcription and cancer. Oncogene *23*, 3208–3216. https://doi.org/10.1038/sj.onc.1207547.
26. White, R.J. (2008). RNA polymerases I and III, non-coding RNAs and cancer. Trends Genet. *24*, 622–629. https://doi.org/10.1016/j.tig.2008.10.003.
27. Johnson, S.A., Dubeau, L., and Johnson, D.L. (2008). Enhanced RNA polymerase III-dependent transcription is required for oncogenic transformation. J. Biol. Chem. *283*, 19184–19191. https://doi.org/10.1074/jbc.M802872200.
28. Goodarzi, H., Nguyen, H.C.B., Zhang, S., Dill, B.D., Molina, H., and Tavazoie, S.F. (2016). Modulated expression of specific tRNAs drives gene expression and cancer progression. Cell *165*, 1416–1427. https://doi.org/10.1016/j.cell.2016.05.046.

29. Graczyk, D., Cieśla, M., and Boguta, M. (2018). Regulation of tRNA synthesis by the general transcription factors of RNA polymerase III - TFIIIB and TFIIIC, and by the MAF1 protein. Biochim. Biophys. Acta Gene Regul. Mech. *1861*, 320–329. https://doi.org/10.1016/j.bbagrm.2018.01.011.

30. Winter, A.G., Sourvinos, G., Allison, S.J., Tosh, K., Scott, P.H., Spandidos, D.A., and White, R.J. (2000). RNA polymerase III transcription factor TFIIIC2 is overexpressed in ovarian tumors. Proc. Natl. Acad. Sci. USA *97*, 12619–12624. https://doi.org/10.1073/pnas.230224097.

31. Ciesla, M., Skowronek, E., and Boguta, M. (2018). Function of TFIIIC, RNA polymerase III initiation factor, in activation and repression of tRNA gene transcription. Nucleic Acids Res. *46*, 9444–9455. https://doi.org/10.1093/nar/gky656.

32. Ferrari, R., de Llobet Cucalon, L.I., Di Vona, C., Le Dilly, F., Vidal, E., Lioutas, A., Oliete, J.Q., Jochem, L., Cutts, E., Dieci, G., et al. (2020). TFIIIC binding to Alu elements controls gene expression via chromatin looping and histone acetylation. Mol. Cell *77*, 475–487.e11. https://doi.org/10.1016/j.molcel.2019.10.020.

33. Moqtaderi, Z., Wang, J., Raha, D., White, R.J., Snyder, M., Weng, Z., and Struhl, K. (2010). Genomic binding profiles of functionally distinct RNA polymerase III transcription complexes in human cells. Nat. Struct. Mol. Biol. *17*, 635–640. https://doi.org/10.1038/nsmb.1794.

34. Moqtaderi, Z., and Struhl, K. (2004). Genome-wide occupancy profile of the RNA polymerase III machinery in Saccharomyces cerevisiae reveals loci with incomplete transcription complexes. Mol. Cell. Biol. *24*, 4118–4127. https://doi.org/10.1128/MCB.24.10.4118-4127.2004.

35. Rozenfeld, S., and Thuriaux, P. (2001). Genetic interactions within TFIIIC, the promoter-binding factor of yeast RNA polymerase III. Mol. Genet. Genomics *265*, 705–710. https://doi.org/10.1007/s004380100467.

36. Nagarajavel, V., Iben, J.R., Howard, B.H., Maraia, R.J., and Clark, D.J. (2013). Global 'bootprinting' reveals the elastic architecture of the yeast TFIIIB-TFIIIC transcription complex in vivo. Nucleic Acids Res. *41*, 8135–8143. https://doi.org/10.1093/nar/gkt611.

37. Arrebola, R., Manaud, N., Rozenfeld, S., Marsolier, M.C., Lefebvre, O., Carles, C., Thuriaux, P., Conesa, C., and Sentenac, A. (1998). Tau91, an essential subunit of yeast transcription factor IIIC, cooperates with tau138 in DNA binding. Mol. Cell. Biol. *18*, 1–9. https://doi.org/10.1128/MCB.18.1.1.

38. Dumay-Odelot, H., Acker, J., Arrebola, R., Sentenac, A., and Marck, C. (2002). Multiple roles of the tau131 subunit of yeast transcription factor IIIC (TFIIIC) in TFIIIB assembly. Mol. Cell. Biol. *22*, 298–308. https://doi.org/10.1128/MCB.22.1.298-308.2002.

39. Hsieh, Y.J., Wang, Z., Kovelman, R., and Roeder, R.G. (1999). Cloning and characterization of two evolutionarily conserved subunits (TFIIIC102 and TFIIIC63) of human TFIIIC and their involvement in functional interactions with TFIIIB and RNA polymerase III. Mol. Cell. Biol. *19*, 4944–4952. https://doi.org/10.1128/MCB.19.7.4944.

40. Petes, T.D., Hereford, L.M., and Skryabin, K.G. (1978). Characterization of two types of yeast ribosomal DNA genes. J. Bacteriol. *134*, 295–305. https://doi.org/10.1128/jb.134.1.295-305.1978.

41. Braun, B.R., Riggs, D.L., Kassavetis, G.A., and Geiduschek, E.P. (1989). Multiple states of protein-DNA interaction in the assembly of transcription complexes on Saccharomyces cerevisiae 5S ribosomal RNA genes. Proc. Natl. Acad. Sci. USA *86*, 2530–2534. https://doi.org/10.1073/pnas.86.8.2530.

42. Léveillard, T., Kassavetis, G.A., and Geiduschek, E.P. (1991). Saccharomyces cerevisiae transcription factors IIIB and IIIC bend the DNA of a tRNA(Gln) gene. J. Biol. Chem. *266*, 5162–5168.

43. Brown, M.L., Schroth, G.P., Gottesfeld, J.M., and Bazett-Jones, D.P. (1996). Protein and DNA requirements for the transcription factor IIIA-induced distortion of the 5 S rRNA gene promoter. J. Mol. Biol. *262*, 600–614. https://doi.org/10.1006/jmbi.1996.0539.

44. Braun, B.R., Kassavetis, G.A., and Geiduschek, E.P. (1992). Bending of the Saccharomyces cerevisiae 5S rRNA gene in transcription factor complexes. J. Biol. Chem. *267*, 22562–22569.

45. Bazett-Jones, D.P., and Brown, M.L. (1989). Electron microscopy reveals that transcription factor TFIIIA bends 5S DNA. Mol. Cell. Biol. *9*, 336–341. https://doi.org/10.1128/mcb.9.1.336-341.1989.

46. Sreenivasan, R., Shkel, I.A., Chhabra, M., Drennan, A., Heitkamp, S., Wang, H.C., Sridevi, M.A., Plaskon, D., McNerney, C., Callies, K., et al. (2020). Fluorescence-detected conformational changes in duplex DNA in open complex formation by Escherichia coli RNA polymerase: upstream wrapping and downstream bending precede clamp opening and insertion of the downstream duplex. Biochemistry *59*, 1565–1581. https://doi.org/10.1021/acs.biochem.0c00098.

47. Braun, B.R., Bartholomew, B., Kassavetis, G.A., and Geiduschek, E.P. (1992). Topography of transcription factor complexes on the Saccharomyces cerevisiae 5 S RNA gene. J. Mol. Biol. *228*, 1063–1077. https://doi.org/10.1016/0022-2836(92)90315-b.

48. Bartholomew, B., Kassavetis, G.A., and Geiduschek, E.P. (1991). Two components of Saccharomyces cerevisiae transcription factor IIIB (TFIIIB) are stereospecifically located upstream of a tRNA gene and interact with the second-largest subunit of TFIIIC. Mol. Cell. Biol. *11*, 5181–5189. https://doi.org/10.1128/mcb.11.10.5181-5189.1991.

49. Huang, Y., Hamada, M., and Maraia, R.J. (2000). Isolation and cloning of four subunits of a fission yeast TFIIIC complex that includes an ortholog of the human regulatory protein TFIIICbeta. J. Biol. Chem. *275*, 31480–31487. https://doi.org/10.1074/jbc.M004635200.

50. Rowland, O., and Segall, J. (1996). Interaction of wild-type and truncated forms of transcription factor IIIA from Saccharomyces cerevisiae with the 5 S RNA gene. J. Biol. Chem. *271*, 12103–12110. https://doi.org/10.1074/jbc.271.20.12103.

51. Milne, C.A., and Segall, J. (1993). Mapping regions of yeast transcription factor IIIA required for DNA binding, interaction with transcription factor IIIC, and transcription activity. J. Biol. Chem. *268*, 11364–11371.

52. Del Rio, S., and Setzer, D.R. (1993). The role of zinc fingers in transcriptional activation by transcription factor IIIA. Proc. Natl. Acad. Sci. USA *90*, 168–172. https://doi.org/10.1073/pnas.90.1.168.

53. Wuttke, D.S., Foster, M.P., Case, D.A., Gottesfeld, J.M., and Wright, P.E. (1997). Solution structure of the first three zinc fingers of TFIIIA bound to the cognate DNA sequence: determinants of affinity and sequence specificity. J. Mol. Biol. *273*, 183–206. https://doi.org/10.1006/jmbi.1997.1291.

54. Hayes, J., Tullius, T.D., and Wolffe, A.P. (1989). A protein-protein interaction is essential for stable complex formation on a 5 S RNA gene. J. Biol. Chem. *264*, 6009–6012.

55. Rothfels, K., Rowland, O., and Segall, J. (2007). Zinc fingers 1 and 7 of yeast TFIIIA are essential for assembly of a functional transcription complex on the 5 S RNA gene. Nucleic Acids Res. *35*, 4869–4881. https://doi.org/10.1093/nar/gkm517.

56. Rowland, O., and Segall, J. (1998). A hydrophobic segment within the 81-amino-acid domain of TFIIIA from Saccharomyces cerevisiae is essential for its transcription factor activity. Mol. Cell. Biol. *18*, 420–432. https://doi.org/10.1128/MCB.18.1.420.

57. Bieker, J.J., Martin, P.L., and Roeder, R.G. (1985). Formation of a rate-limiting intermediate in 5S RNA gene transcription. Cell *40*, 119–127. https://doi.org/10.1016/0092-8674(85)90315-0.

58. Carey, M.F., Gerrard, S.P., and Cozzarelli, N.R. (1986). Analysis of RNA polymerase III transcription complexes by gel filtration. J. Biol. Chem. *261*, 4309–4317.

59. Clemens, K.R., Liao, X., Wolf, V., Wright, P.E., and Gottesfeld, J.M. (1992). Definition of the binding sites of individual zinc fingers in the transcription factor IIIA-5S RNA gene complex. Proc. Natl. Acad. Sci. USA *89*, 10822–10826. https://doi.org/10.1073/pnas.89.22.10822.

60. Hayes, J.J., and Clemens, K.R. (1992). Locations of contacts between individual zinc fingers of Xenopus laevis transcription factor IIIA and the

internal control region of a 5S RNA gene. Biochemistry *31*, 11600–11605. https://doi.org/10.1021/bi00161a045.

61. Joazeiro, C.A., Kassavetis, G.A., and Geiduschek, E.P. (1996). Alternative outcomes in assembly of promoter complexes: the roles of TBP and a flexible linker in placing TFIIIB on tRNA genes. Genes Dev. *10*, 725–739. https://doi.org/10.1101/gad.10.6.725.
62. Kassavetis, G.A., Joazeiro, C.A., Pisano, M., Geiduschek, E.P., Colbert, T., Hahn, S., and Blanco, J.A. (1992). The role of the TATA-binding protein in the assembly and function of the multisubunit yeast RNA polymerase III transcription factor, TFIIIB. Cell *71*, 1055–1064. https://doi.org/10.1016/0092-8674(92)90399-w.
63. Geiduschek, E.P., and Kassavetis, G.A. (2001). The RNA polymerase III transcription apparatus. J. Mol. Biol. *310*, 1–26. https://doi.org/10.1006/jmbi.2001.4732.
64. Chaussivert, N., Conesa, C., Shaaban, S., and Sentenac, A. (1995). Complex interactions between yeast TFIIIB and TFIIIC. J. Biol. Chem. *270*, 15353–15358. https://doi.org/10.1074/jbc.270.25.15353.
65. Moir, R.D., Puglia, K.V., and Willis, I.M. (2000). Interactions between the tetratricopeptide repeat-containing transcription factor TFIIIC131 and its ligand, TFIIIB70. Evidence for a conformational change in the complex. J. Biol. Chem. *275*, 26591–26598. https://doi.org/10.1074/jbc.M003991200.
66. Liao, Y., Moir, R.D., and Willis, I.M. (2006). Interactions of Brf1 peptides with the tetratricopeptide repeat-containing subunit of TFIIIC inhibit and promote preinitiation complex assembly. Mol. Cell. Biol. *26*, 5946–5956. https://doi.org/10.1128/MCB.00689-06.
67. Moir, R.D., Sethy-Coraci, I., Puglia, K., Librizzi, M.D., and Willis, I.M. (1997). A tetratricopeptide repeat mutation in yeast transcription factor IIIC131 (TFIIIC131) facilitates recruitment of TFIIB-related factor TFIIIB70. Mol. Cell. Biol. *17*, 7119–7125. https://doi.org/10.1128/MCB.17.12.7119.
68. Kassavetis, G.A., Riggs, D.L., Negri, R., Nguyen, L.H., and Geiduschek, E.P. (1989). Transcription factor IIIB generates extended DNA interactions in RNA polymerase III transcription complexes on tRNA genes. Mol. Cell. Biol. *9*, 2551–2566. https://doi.org/10.1128/mcb.9.6.2551-2566.1989.
69. Rhodes, D. (1985). Structural analysis of a triple complex between the histone octamer, a Xenopus gene for 5S RNA and transcription factor IIIA. EMBO J. *4*, 3473–3482. https://doi.org/10.1002/j.1460-2075.1985.tb04106.x.
70. Gottesfeld, J.M. (1987). DNA sequence-directed nucleosome reconstitution on 5S RNA genes of Xenopus laevis. Mol. Cell. Biol. *7*, 1612–1622. https://doi.org/10.1128/mcb.7.5.1612-1622.1987.
71. Kassavetis, G.A., Soragni, E., Driscoll, R., and Geiduschek, E.P. (2005). Reconfiguring the connectivity of a multiprotein complex: fusions of yeast TATA-binding protein with Brf1, and the function of transcription factor IIIB. Proc. Natl. Acad. Sci. USA *102*, 15406–15411. https://doi.org/10.1073/pnas.0507653102.
72. Suloway, C., Pulokas, J., Fellmann, D., Cheng, A., Guerra, F., Quispe, J., Stagg, S., Potter, C.S., and Carragher, B. (2005). Automated molecular microscopy: the new Leginon system. J. Struct. Biol. *151*, 41–60. https://doi.org/10.1016/j.jsb.2005.03.010.
73. Voss, N.R., Yoshioka, C.K., Radermacher, M., Potter, C.S., and Carragher, B. (2009). DoG Picker and TiltPicker: software tools to facilitate particle selection in single particle electron microscopy. J. Struct. Biol. *166*, 205–213. https://doi.org/10.1016/j.jsb.2009.01.004.
74. Lander, G.C., Stagg, S.M., Voss, N.R., Cheng, A., Fellmann, D., Pulokas, J., Yoshioka, C., Irving, C., Mulder, A., Lau, P.W., et al. (2009). Appion: an integrated, database-driven pipeline to facilitate EM image processing. J. Struct. Biol. *166*, 95–102. https://doi.org/10.1016/j.jsb.2009.01.002.
75. Tang, G., Peng, L., Baldwin, P.R., Mann, D.S., Jiang, W., Rees, I., and Ludtke, S.J. (2007). EMAN2: an extensible image processing suite for electron microscopy. J. Struct. Biol. *157*, 38–46. https://doi.org/10.1016/j.jsb.2006.05.009.
76. Zivanov, J., Nakane, T., and Scheres, S.H.W. (2020). Estimation of high-order aberrations and anisotropic magnification from cryo-EM data sets in RELION-3.1. IUCrJ *7*, 253–267. https://doi.org/10.1107/S2052252520000081.
77. Rohou, A., and Grigorieff, N. (2015). CTFFIND4: fast and accurate defocus estimation from electron micrographs. J. Struct. Biol. *192*, 216–221. https://doi.org/10.1016/j.jsb.2015.08.008.
78. Punjani, A., Rubinstein, J.L., Fleet, D.J., and Brubaker, M.A. (2017). cryoSPARC: algorithms for rapid unsupervised cryo-EM structure determination. Nat. Methods *14*, 290–296. https://doi.org/10.1038/nmeth.4169.
79. Sanchez-Garcia, R., Gomez-Blanco, J., Cuervo, A., Carazo, J.M., Sorzano, C.O.S., and Vargas, J. (2021). DeepEMhancer: a deep learning solution for cryo-EM volume post-processing. Commun. Biol. *4*, 874. https://doi.org/10.1038/s42003-021-02399-1.
80. Jumper, J., Evans, R., Pritzel, A., Green, T., Figurnov, M., Ronneberger, O., Tunyasuvunakool, K., Bates, R., Žídek, A., Potapenko, A., et al. (2021). Highly accurate protein structure prediction with AlphaFold. Nature *596*, 583–589. https://doi.org/10.1038/s41586-021-03819-2.
81. Emsley, P., and Cowtan, K. (2004). Coot: model-building tools for molecular graphics. Acta Crystallogr. D Biol. Crystallogr. *60*, 2126–2132. https://doi.org/10.1107/S0907444904019158.
82. Pettersen, E.F., Goddard, T.D., Huang, C.C., Couch, G.S., Greenblatt, D.M., Meng, E.C., and Ferrin, T.E. (2004). UCSF Chimera–a visualization system for exploratory research and analysis. J. Comput. Chem. *25*, 1605–1612. https://doi.org/10.1002/jcc.20084.
83. Pettersen, E.F., Goddard, T.D., Huang, C.C., Meng, E.C., Couch, G.S., Croll, T.I., Morris, J.H., and Ferrin, T.E. (2021). UCSF ChimeraX: structure visualization for researchers, educators, and developers. Protein Sci. *30*, 70–82. https://doi.org/10.1002/pro.3943.
84. Croll, T.I. (2018). Isolde: a physically realistic environment for model building into low-resolution electron-density maps. Acta Crystallogr. D Struct. Biol. *74*, 519–530. https://doi.org/10.1107/S2059798318002425.
85. Afonine, P.V., Poon, B.K., Read, R.J., Sobolev, O.V., Terwilliger, T.C., Urzhumtsev, A., and Adams, P.D. (2018). Real-space refinement in PHENIX for cryo-EM and crystallography. Acta Crystallogr. D Struct. Biol. *74*, 531–544. https://doi.org/10.1107/S2059798318006551.
86. Ashkenazy, H., Abadi, S., Martz, E., Chay, O., Mayrose, I., Pupko, T., and Ben-Tal, N. (2016). ConSurf 2016: an improved methodology to estimate and visualize evolutionary conservation in macromolecules. Nucleic Acids Res. *44*, W344–W350. https://doi.org/10.1093/nar/gkw408.
87. Ogura, T., Iwasaki, K., and Sato, C. (2003). Topology representing network enables highly accurate classification of protein images taken by cryo electron-microscope without masking. J. Struct. Biol. *143*, 185–200. https://doi.org/10.1016/j.jsb.2003.08.005.
88. Patel, A., Toso, D., Litvak, A., and Nogales, E. (2021). Efficient graphene oxide coating improves cryo-EM sample preparation and data collection from tilted grids. Preprint at bioRxiv. https://doi.org/10.1101/2021.03.08.434344.
89. Mastronarde, D.N. (2005). Automated electron microscope tomography using robust prediction of specimen movements. J. Struct. Biol. *152*, 36–51. https://doi.org/10.1016/j.jsb.2005.07.007.
90. Henderson, R., Sali, A., Baker, M.L., Carragher, B., Devkota, B., Downing, K.H., Egelman, E.H., Feng, Z., Frank, J., Grigorieff, N., et al. (2012). Outcome of the first electron microscopy validation task force meeting. Structure *20*, 205–214. https://doi.org/10.1016/j.str.2011.12.014.
91. Banerjee, C., Liauw, B.W., and Vafabakhsh, R. (2022). Visualizing the conformational dynamics of membrane receptors using single-molecule FRET. J. Vis. Exp. https://doi.org/10.3791/64254.
92. van de Meent, J.W., Bronson, J.E., Wiggins, C.H., and Gonzalez, R.L., Jr. (2014). Empirical Bayes methods enable advanced population-level analyses of single-molecule RET experiments. Biophys. J. *106*, 1327–1337. https://doi.org/10.1016/j.bpj.2013.12.055.

STAR★METHODS

KEY RESOURCES TABLE

REAGENT or RESOURCE	SOURCE	IDENTIFIER
Bacterial and virus strains		
E. coli BL21 (DE3) pRARE	Invitrogen	N/A
Chemicals, peptides, and recombinant proteins		
S. cerevisiae TFIIIA	This study	N/A
S. cerevisiae TFIIIC	Han et al.[19]	N/A
Brf1N-TBPc-Brf1C	Kassavetis et al.[71]	N/A
His-Pur Ni-NTA resin	Fisher Scientific	Cat#: 88221
IgG Sepharose 6 Fast Flow affinity resin	Cytiva	Cat#: 17096901
TEV protease	Han et al.[19]	N/A
Calmodulin Affinity Resin	Agilent Technologies	Cat#: 214303-52
EcoRI-HF	New England Biolabs	Cat#: R3101T
Glutaraldehyde 25%	Sigma-Aldrich	Cat#: G5882
Nonidet P40 Substitute	Roche	Cat#: 11754599001
Dynabeads Streptavidin T1	Fisher Scientific	Cat#: 65602
NHS ester-conjugated Cy3 dye	Click Chemistry Tools	Cat#: 1075-1
NHS ester-conjugated Cy5 dye	Click Chemistry Tools	Cat#: 1076-1
mPEG	Laysan Bio	Cat#: MPEG-SIL-5000
biotin-PEG 1% (w/w)	Laysan Bio	Cat#: Biotin-PEG-SVA-5000
NeutrAvidin	ThermoFisher Scientific	Cat#: 31000
Trolox	Sigma	Cat#: 53188-07
protocatechuic acid	Sigma	Cat#: 03930590
bacterial protocatechuate 3,4-dioxygenase (rPCO)	Oriental Yeast	Cat#: 46852004
Deposited data		
TFIIIA-TFIIIC-Brf1-TBP cryo-EM globally refined map	This study	EMDB: 29071
Brf1-TBP-DNA cryo-EM focused refined map	This study	EMDB: 29356
TFIIIA-TFIIIC cryo-EM globally refined map	This study	EMDB: 29358
TFIIIA-TFIIIC-Brf1-TBP model	This study	PDB: 8FFZ
Experimental models: Cell lines		
S. cerevisiae TAP tagged TFC8 (YPL007C) Strain	GE Dharmacon	Cat#: YSC1178-202233621
Oligonucleotides		
5S rRNA gene construct, cryo-EM, sense 5'-/5BiotinTEG/TACGGACCATGGAA TTCCCCAGT AACATGTCTGGACCC TGCCCTCATATCACCTGCGTTTCCG TTAAACTATCGGTTGCGGCCATATC TACCAGAAAGCACCGTTTCCCGTCCGA TCAACTGTAGTTAAGCTGGTAAGAGCC TGACCGAGTAGTGTAGTGGGTGACCA TACGCGAAACTCAGGTGCTGCAATCT -3'	This study	Integrated DNA Technologies

(*Continued on next page*)

Continued

REAGENT or RESOURCE	SOURCE	IDENTIFIER
5S rRNA gene construct, cryo-EM, antisense 5'- AGATTGCAGCACCTGAG TTTCGCGTATGGTCACCCACTACACTAC TCGGTCAGGCTCTTACCAGCTTAAC TACAGTTGATCGGACGGGAAACGGTGC TTTCTGGTAGATATGGCCGCAACCGA TAGTTTAACGGAAACGCAGGTGATA TGAGGGCAGGGTCCAGACATGTTAC TGGGGAATTCCATGGTCCGTA -3'	This study	Integrated DNA Technologies
5S rRNA gene construct, smFRET, sense 5'- AACATGTCTGGACCCTGCCCTCATA TCACCTGCGTTTCCGTTAAACTATCGG TTGCGGCCATATCTACCAGAAAGCACC GTTTCCCGTCCGATCAACTGTAGTTAA GCTGGTAAGAGCCTGACCGAGTAGTG TAGTGGG/iAmMC6dT/GACCATACGC GAAACTCAGGTGCTGCAATCTGTAGA TTCATTGGACTGGTG-3'	This study	Genscript
5S rRNA gene construct, smFRET, antisense 5'-AGATTGCAGCACCTGAG TTTCGCGTATGGTCACCCACTACAC TACTCGGTCAGGCTCTTACCAGCTT AACTACAGTTGATCGGACGGGAAA CGGTGCTTTCTGGTAGATA/iAmMC6dT/ GGCCGCAACCGATAGTTTAACG GAAACGCAGGTGATATGAGGGCAG GGTCCAGACATGTTACTGGGGAATT CCATGGTCCGTA-3'	This study	Genscript
5S rRNA gene construct, smFRET, sense, biotinylated 5'-/5BiotinTEG/ TACGGACCATGGAATTCCCCAGT-3'	This study	Integrated DNA Technologies
5S rRNA gene construct, smFRET, sense, biotinylated 5'-/5BiotinTEG/ CACCAGTCCAATGAATCTAC-3'	This study	Integrated DNA Technologies
Software and algorithms		
Leginon 3.0	Suloway et al.[72]	http://leginon.org
DogPicker	Voss et al.[73]	https://emg.nysbc.org/redmine/projects/software/wiki/DoGpicker
Appion 3.0	Lander et al.[74]	http://www.appion.org
EMAN2	Tang et al.[75]	https://blake.bcm.edu/emanwiki/EMAN2
RELION 3.1	Zivanov et al.[76]	https://github.com/3dem/relion
Gautomatch	K. Zhang, MRC Laboratory of Molecular Biology, Cambridge, UK	https://lab.rockefeller.edu/chen/assets/file/Gautomatch_Brief_Manual.pdf
CTFFIND 4.1	Rohou and Grigorieff[77]	https://grigoriefflab.umassmed.edu/ctffind4
cryoSPARC 3.2.0	Punjani et al.[78]	https://cryosparc.com/
DeepEMhancer	Sanchez-Garcia et al.[79]	https://github.com/rsanchezgarc/deepEMhancer
Alphafold 2	Jumper et al.[80]	https://alphafold.ebi.ac.uk/
Coot 0.9	Emsley and Cowtan[81]	https://www2.mrc-lmb.cam.ac.uk/personal/pemsley/coot/
UCSF Chimera	Pettersen et al.[82]	https://www.cgl.ucsf.edu/chimera/
UCSF Chimera X 1.4	Pettersen et al.[83]	https://www.cgl.ucsf.edu/chimerax/

(*Continued on next page*)

Continued

REAGENT or RESOURCE	SOURCE	IDENTIFIER
ISOLDE 1.4	Croll[84]	https://isolde.cimr.cam.ac.uk/
PHENIX 1.20.1	Afonine et al.[85]	http://www.phenix-online.org/
ConSurf	Ashkenazy et al.[86]	https://consurf.tau.ac.il/consurf_index.php
Other		
BeadBeater	Biospec Products	Cat#: 1107900-110
400 mesh copper grids	Electron Microscopy Sciences	Cat#: NC1380831
Quantifoil 2/1 300 mesh copper grids	Electron Microscopy Sciences	Cat#: X-102-Cu300
Solarus plasma cleaner 950	Gatan	N/A
Vitrobot Mark IV	Thermo Fisher Scientific	N/A
Jeol 1400	Jeol	N/A
Titan Krios	FEI/Thermo Fisher Scientific	N/A
K3 Summit Direct Electron Detector	Gatan	N/A
Quantum energy filter	Gatan	N/A

RESOURCE AVAILABILITY

Lead contact

Correspondence and requests for materials should be addressed to Yuan He (yuanhe@northwestern.edu).

Materials availability

Materials are available from Yuan He upon request.

Data and code availability

Electron density map and coordinates for the TFIIIA-TFIIIC-Brf1-TBP complex bound to 5S rRNA gene have been deposited in the Electron Microscopy Data Bank (EMDB) with ID code EMDB-29071 and the Protein Data Bank (PDB) with ID code 8FFZ, respectively. Electron density map for the focused refinement on the Brf1-TBP-DNA has been deposited in the EMDB with ID code EMDB-29356. Electron density map for the TFIIIA-TFIIIC complex bound to 5S rRNA gene has been deposited in the EMDB with ID code 29358. All data are publicly available as of the date of publication. Accession numbers and DOI are listed in the key resources table.

This paper does not report original code.

Any additional information required to reanalyze the data reported in this paper is available from the lead contact upon request.

EXPERIMENTAL MODEL AND STUDY PARTICIPANT DETAILS

E. coli cells used in this study were grown in LB medium at 37 °C.

S. cerevisiae strain used in this study were cultured in YPD medium at 30 °C.

METHOD DETAILS

Purification of TFIIIA

Two liters of transformed BL21 (DE3) pRARE cells were grown in LB at 37 °C to an OD600 of 0.6. Then 50 μM $ZnSO_4$ was added, the cells were induced with 1 mM IPTG, and the protein was expressed for two hours at 37 °C. Cells were pelleted for 20 minutes at 4000 x g and resuspended in 40 mL of buffer A (20mM HEPES 7.6, 250 mM NaCl, 5 mM $MgCl_2$, 50 μM ZnSO4, 10% glycerol, 5mM dithiothreitol [DTT], 1 mM phenylmethylsulfonyl fluoride [PMSF]). After cell lysis by sonication, cell pellet was collected by centrifugation for 10 minutes at 4000 x g. The pellet was resuspended in buffer A + 5M urea, then briefly sonicated again and incubated on nutator overnight at 4 °C. Next day, cell debris was removed by centrifugation at 15000 x g at 4 °C for 30 minutes and the supernatant was filtered. The supernatant was loaded twice onto a gravity column with 1 ml of HIS-Select Nickel Affinity Gel (Sigma-Aldrich) equilibrated with buffer A + 5M urea + 20mM imidazole. The resin was washed six times with 2 ml of buffer A + 5M urea + 20mM imidazole. The protein was eluted in 1 ml fractions using buffer A + 5M urea + 300mM imidazole. Fractions containing TFIIIA were pooled together and diluted in three steps over 45 minutes with Buffer A + 1mM PMSF + 5mM DTT. The diluted protein was dialyzed against 1L of Buffer A + 1mM PMSF + 10mM BME in 3.5kDa cut-off snakeskin tubing (Thermo Fisher) overnight at 4 °C. Next day aggregation was removed by centrifugation at 10000 x g for 5 minutes. Supernatant containing refolded TFIIIA was flash-frozen in liquid nitrogen.

Purification of TFIIIC

TFIIIC was purified from an *S. cerevisiae* strain with a TAP tag at the C terminus of τ60 (GE Dharmacon, YSC1178-202233621). Eight liters of yeast were grown overnight. Cells were harvested by centrifugation and resuspended in 200ml of cold TAP extraction buffer (40 mM HEPES pH 8, 250 mM ammonium sulfate, 1 mM EDTA, 10% glycerol, 0.1% Tween-20, 1 mM DTT, 1 mM PMSF, 2mM benzamidine, 0.3 μg/ml leupeptin, 1.4 μg/ml pepstatin, 2 μg/ml chymostatin). Cells were lysed using BeadBeater (Biospec Products). Cell debris was removed by centrifugation at 15000 x g at 4 °C for two hours. The lysate was incubated with 2ml of IgG Sepharose beads (Cytiva) for two hours at 4 °C. The beads were washed and resuspended in 4ml of cold TEV cleavage buffer (10 mM HEPES pH 8, 200 mM NaCl, 0.1% NP-40, 0.5 mM EDTA, 10% glycerol). TEV cleavage was performed using 25 μg of TEV protease at room temperature (RT) for one hour. TEV flowthrough was collected and $CaCl_2$ was added for a final concentration of 2 mM. 800 μl of Calmodulin Affinity Resin (Agilent Technologies) was washed with Calmodulin binding buffer (15 mM HEPES pH 8, 1 mM magnesium acetate, 1 mM imidazole, 2 mM CaCl2, 0.1% NP-40, 10% glycerol, 200 mM ammonium sulfate, 1 mM DTT, 1 mM PMSF, 2mM benzamidine, 0.3 μg/ml leupeptin, 1.4 μg/ml pepstatin, 2 μg/ml chymostatin) and incubated with TEV flowthrough overnight at 4 °C. Following incubation, the beads were washed with Calmodulin binding buffer, followed by Calmodulin wash buffer (same as the binding buffer but with 0.05% NP-40), followed by Calmodulin transfer buffer (same as wash buffer but without $CaCl_2$). 400 μl of Calmodulin elution buffer (15 mM HEPES pH 8, 1 mM magnesium acetate, 1 mM imidazole, 5 mM EGTA, 10% glycerol, 0.05% NP-40, 200 mM ammonium sulfate) was added to the beads and incubated for 45 minutes at 4 °C. First, 400 μl fraction was eluted, another 400 μl of elution buffer was added to the beads, and eluted after 5 minutes. The following fractions were eluted immediately. Fractions containing protein were pooled together, concentrated and flash-frozen in liquid nitrogen.

Purification of Brf1-TBP

The chimera protein Brf1N-TBPc-Brf1C[71] was purified as follows. Two liters of transformed BL21 (DE3) pRARE cells were grown in LB at 37 °C to an OD600 of 0.6, the cells were induced using 0.5 mM IPTG, and the protein was expressed overnight at 18 °C. Cells were harvested by centrifugation and resuspended in 35 ml of BT lysis buffer (20 mM HEPES pH 7.6, 25 μM EDTA, 1.14 M NaCl, 5% glycerol, 10 EDTA, 1.14 M NaPMSF, 1 μg/ml leupeptin, 1 μg/ml pepstatin, 300 μg/ml lysozyme), followed by incubation on ice for one hour and followed by sonication. Cell debris was removed by centrifugation at 13000 x g at 4 °C for one hour. The lysate was loaded onto a gravity column with 500 μl of His-Pur Ni-NTA resin (Fisher Scientific) equilibrated with BT lysis buffer. The resin was washed five times with 1 ml of BT wash buffer 1 (20 mM HEPES pH 7.6, 7 mM MgCl2, 0.5 M NaCl, 10 mM imidazole, 5% glycerol, 10 mM BME, 0.5 mM PMSF, 1 μg/ml leupeptin, 1 μg/ml pepstatin) and five times with 1 ml of BT wash buffer 2 (20 mM HEPES pH 7.6, 7 mM MgCl2, 0.5 M NaCl, 20 mM imidazole, 5% glycerol, 10 mM BME, 0.5 mM PMSF, 1 μg/ml leupeptin, 1 μg/ml pepstatin). Protein was eluted in five 1 ml fractions with BT elution buffer (20 mM HEPES pH 7.6, 7 mM MgCl2, 0.5 M NaCl, 200 mM imidazole, 5% glycerol, 10 mM BME, 0.5 mM PMSF, 1 μg/ml leupeptin, 1 μg/ml pepstatin). Fractions containing Brf1-TBP were pooled and dialyzed against 500 ml of dialysis buffer (20mM HEPES pH 7.6, 200mM NaCl, 7mM MgCl2, 0.01% Tween-20, 10% glycerol, 0.2mM PMSF, 10mM BME) in 12 kDa Pur-A-Lyzer Maxi (SigmaAldrich) overnight at 4 °C. Next day the dialysis buffer was replaced with fresh dialysis buffer and the protein was dialyzed for another 5 hours. Fractions containing protein were pooled together and flash-frozen in liquid nitrogen.

Complex assembly

First, 2 pmol of 5S rRNA gene DNA template (sense: 5'-/5BiotinTEG/TACGGACCATGGAATTCCCCAGT AACATGTCTGGACCCTG CCCTCATATCACCTGCGTTTCCGTTAAACTATCGGTTGCGGCCATATCTACCAGAAAGCACCGTTTCCCGTCCGATCAACTGTAGT TAAGCTGGTAAGAGCCTGACCGAGTAGTGTAGTGGGTGACCATACGCGAAACTCAGGTGCTGCAATCT -3', antisense: 5'- AGATT GCAGCACCTGAGTTTCGCGTATGGTCACCCACTACACTACTCGGTCAGGCTCTTACCAGCTTAACTACAGTTGATCGGACGGGAA ACGGTGCTTTCTGGTAGATATGGCCGCAACCGATAGTTTAACGGAAACGCAGGTGATATGAGGGCAGGGTCCAGACATGTTACTG GGGAATTCCATGGTCCGTA -3') was mixed with 100 nmol TFIIIA and incubated at RT for 5 minutes. Then 200 nmol TFIIIC was added and incubated at RT for 5 minutes. For the TFIIIA-TFIIIC-Brf1-TBP complex, the previous step was followed by the addition of 150 nmol Brf1-TBP. The salt concentration was adjusted to 100 mM KCl with the addition of buffer 1 (12 mM HEPES pH 7.6, 0.12 mM EDTA, 12% glycerol, 8.25 mM $MgCl_2$, 1 mM DTT, and 0.05% NP-40). All components were incubated for an additional 5 minutes at RT before binding to T1 streptavidin beads (Fisher Scientific) at RT for 15 minutes. Assembled complexes were washed with buffer 2 (10 mM HEPES pH 7.6, 10 mM Tris pH 7.6, 5% glycerol, 5 mM $MgCl_2$, 50 mM KCl, 1 mM DTT, and 0.05% NP-40) and eluted with buffer 3 (10 mM HEPES pH 7.6, 5% glycerol, 10 mM $MgCl_2$, 50 mM KCl, 1 mM DTT, 0.05% NP-40, and 30 units EcoRI-HF (New England Biolabs).

Negative stain EM data collection and processing

Negative stain samples were prepared using 400 mesh copper grids (Electron Microscopy Sciences) coated with continuous carbon on a nitrocellulose support film. Before usage, they were glow-discharged for 10 seconds with 25 W of power using the Solarus plasma cleaner 950 (Gatan). Purified TFIIIA-TFIIIC and TFIIIA-TFIIIC-Brf1-TBP complexes in buffer 4 were cross-linked with 0.05% glutaraldehyde for 10 minutes on ice and incubated for 10 minutes on a grid in a homemade humidity chamber at 4 °C. The grid was stained on four 40 μL drops of 2% uranyl formate solution for 5, 10, 15, and 20 seconds sequentially and blotted dry

with #1 filter paper (Whatman). Images were collected on a Jeol 1400 microscope equipped with a Gatan 4k × 4x CCD camera at 30,000x magnification (3.71 Å/pixel), a defocus range of -1.5 to -3 μm, and 20 $e^-/Å^2$ total electron dose using Leginon.[72]

Particles were picked using DogPicker, extracted, and 2D classified using iterative MSA/MRA topological alignment within the Appion data processing software.[73,74,77,87] A particle stack of ~50,000 particles with a box size of 96 x 96 pixels was subjected to iterative, multi-reference projection-matching 3D refinement using EMAN2 software package to generate an initial reference for cryo-EM data processing.[75]

Cryo-EM sample preparation

Cryo-EM samples were prepared using Quantifoil 2/1 300 mesh copper grids (EMS). Grids were glow discharged for 10 seconds with 25 W of power using the Solarus plasma cleaner 950 (Gatan), and then a thin layer of graphene oxide was applied as described previously.[88] Purified TFIIIA-TFIIIC and TFIIIA-TFIIIC-Brf1-TBP samples (~3.5 μL) were incubated with 0.05% glutaraldehyde for 10 minutes on ice. The sample was applied to a grid in a Vitrobot Mark IV (Thermo Fisher Scientific) operating at 4 °C with 100% humidity. After 5 minutes of incubation, the sample was blotted with 10 force for four seconds and immediately plunged into liquid ethane cooled to liquid nitrogen temperature.

Cryo-EM data collection and processing

Cryo-EM data were collected at the Pacific Northwestern Center for Cryo-EM (PNCC). Images were collected using semi-automated data collection in Serial EM[89] on a Titan Krios transmission electron microscope (TEM) operated at 300 keV (Thermo Fisher Scientific), equipped with a Quantum energy filter (Gatan), and with a K3 direct detector (Gatan) operating in super-resolution mode.

For the TFIIIA-TFIIIC sample, images were collected at a magnification of 30,000X (super-resolution mode, 0.5395 Å/pixel for raw data, 1.079 Å/pixel after binning) using a defocus range of -1.5 to -3 μm with a dose rate of 1 e^-/pixel/frame for a total dose of 50 $e^-/Å^2$. A dataset of 11,645 images was collected. For the TFIIIA-TFIIIC-Brf1-TBP sample, images were collected at a magnification of 30,000X (super-resolution mode, 0.528 Å/pixel for raw data, 1.056 Å/pixel after binning) using a defocus range of -2 to -5 μm with a dose rate of 1 e^-/pixel/frame for a total dose of 60 $e^-/Å^2$. A dataset of 23,211 images was collected.

RELION 3.1 was used for all pre-processing, 3D classification, model refinement, post-processing, and local-resolution estimation jobs.[76] Particles were picked using Gautomatch (developed by K. Zhang, MRC Laboratory of Molecular Biology, Cambridge, UK) and Laplacian-of-Gaussian (LoG) picking in RELION 3.1. Duplicated particles were removed. Local CTF of each micrograph was determined using CTFFIND-4.1.[77]

For the TFIIIA-TFIIIC complex, a stack of 2,176,308 particles was binned by a factor of 2 (2.158 Å/pixel) and extracted with a box size of 132 pixels. First round of 3D classification (10 classes) with the negative stain reconstruction as a reference was used to clean up the particle stack. One class of 159,078 particles showed clear structural features of the TFIIIA-TFIIIC complex and was selected for further processing. The selected particles were 3D auto-refined and used in the second round of 3D classification (5 classes). Three classes (109,548) were selected and 3D auto-refined. Another round of 3D auto-refinement was performed with a soft mask, resulting in a 6.78 Å resolution reconstruction. All reported resolutions correspond to the gold-standard Fourier shell correlation (FSC) using the 0.143 criteria.[90] Three rounds of per-particle CTF refinement were performed, followed by Bayesian particle polishing. 3D auto-refinement using the polished particles resulted in a 6.62 Å resolution map.

For the TFIIIA-TFIIIC-Brf1-TBP complex, a stack of 5,748,589 particles was binned by a factor of 2 (2.112 Å/pixel) and extracted with a box size of 132 pixels. First round of 3D classification (10 classes) with the negative stain reconstruction as a reference was used to clean up the particle stack. One class of 665,210 particles showed clear structural features of the TFIIIA-TFIIIC-Brf1-TBP complex and was selected for further processing. The selected particles were 3D auto-refined and used in the second round of 3D classification (3 classes) without alignment. One class (78,512 particles) was selected. The selected particles were 3D auto-refined, re-centered, and re-extracted without binning (1.056 Å/pixel, box size = 264 pixels). Another round of 3D auto-refinement was performed with a soft mask applied around the whole complex, resulting in a 4.36 Å resolution reconstruction. The particle stack was re-extracted with a bigger box size (384 pixels). Three rounds of 3D auto-refinement, per-particle CTF refinement and Bayesian particle polishing were performed. 3D auto-refinement using the polished particles resulted in a 3.83 Å resolution map. To improve the map quality of the Brf1-TBP part, focused 3D variability analysis was performed in cryoSPARC.[78] Briefly, the particle stack that resulted in 4.36 Å resolution reconstruction, was imported into cryoSPARC, where it was used for Non-uniform (NU) refinement, local refinement (soft mask applied to focus on Brf1-TBP-DNA density), signal subtraction and 3D variability analysis in cluster mode. This procedure produced a 7.14 Å resolution reconstruction of Brf1-TBP-DNA density. In parallel with post-processing done in RELION 3.1, DeepEMhancer was used to better correct local B-factors and produced cleaner maps for model building and docking.[79]

Model building and refinement

TFIIIA-TFIIIC-Brf1-TBP model

The resolution of the TFIIIA-TFIIIC-Brf1-TBP complex map (3.8 Å) allowed for AlphaFold-guided model building for the entire complex.[80] AlphaFold pLDDT score (per-residue estimate of the modeling confidence on a scale from 0 – 100) was used as scoring metric for predictions. Alphafold was used to predict individual domains or full subunits of TFIIIA and TFIIIC, and the produced models were fitted as a rigid body into the density map using UCSF Chimera.[82] Published experimental structures were used in rigid body fitting as well (Table 2). Side chains were not stubbed. Side chain orientations from Alphafold predictions or experimental models were kept in

cases, where map quality did not allow to distinguish a side chain orientation. Manual adjustments were made in Coot[81] and ISOLDE.[84] The final model was refined in Phenix.[85] The refined model was inspected with the help of ISOLDE, where clashes and rotamer outliers were resolved.

TFIIIA

X. laevis structure of ZF 1 to 3 bound to DNA (PDB:1TF3) was fitted as rigid body into the TFIIIA density. *S. cerevisiae* TFIIIA Alphafold prediction was aligned with the experimental *X. laevis* structure, and individual ZF was fitted as rigid body into the TFIIIA density. Predicted regions that were not visible in the density were trimmed.

TFIIIC

The structure of the subcomplex of τ60 and τ91 (PDB: 2J04) was fitted as rigid body into the density. *S. cerevisiae* Alphafold predictions for τ60 and τ91 were aligned with the experimental structure, and flexible loops, not visible in the density, were trimmed. The cryo-EM structure of the τA lobe comprised of τ131, τ95 and τ55 subunits (PDB: 6YJ6) was fitted as rigid body. Alphafold predictions were aligned with subunits and manually adjusted. Predicted regions that were not visible in the density were trimmed. For τ138, individual folded domains from Alphafold prediction were fitted as rigid body into the map, and connecting linkers were manually adjusted.

Brf1-TBP

Brf1-TBP model from *S. cerevisiae* Pol III PIC structure (PDB:6CNB) was fitted into Brf1-TBP density as rigid body, and flexibly tethered domains of Brf1 that could not be traced in the density (cyclin fold 1 and zinc ribbon), were trimmed. This model was not manually adjusted due to low resolution of the map in this area.

DNA

Double strand DNA model with 5S rRNA gene sequence was generated using webserver (http://www.scfbio-iitd.res.in/software/drugdesign/bdna.jsp). The DNA register was traced using sequence alignment between *X. laevis* and *S. cerevisiae* ICR and structure of *X. laevis* structure of ZF 1 to 3 bound to DNA (PDB:1TF3), as well as the positioning of Brf1-TBP at the upstream region. The DNA was fitted into the density in ISOLDE.

TFIIIA-TFIIIC model

The model of the TFIIIA-TFIIIC-Brf1-TBP complex was fitted in the density map of the TFIIIA-TFIIIC complex. TFIIIC subunits τ55, τ95, τ91, and τ60 completely fit in the map. Protein-DNA contacts within the τB model are identical as well. C-terminal TPR and helical domains of τ131 are placed identically to the TFIIIA-TFIIIC-Brf1-TBP complex. N-terminal TPR cannot be resolved, but low-resolution features suggested a conformation of τ131, similar to the one in τA lobe structure (PDB: 6YJ6). TFIIIA zinc fingers 1-5 interact with DNA, while zinc fingers 6-8 protrude away from the DNA. The overall position of TFIIIA is identical to the TFIIIA-TFIIIC-Brf1-TBP complex; however, zinc finger 9 and adjacent helix are not visible in the map. DNA in this complex is also positioned identically to the TFIIIA-TFIIIC-Brf1-TBP complex.

UCSF Chimera and UCSF Chimera X were used for figure and movie generation.[82,83] ConSurf web server was used for estimating the evolutionary conservation of residues.[86]

Preparation of DNA constructs for smFRET

The PAGE-purified DNA oligonucleotides containing biotin for immobilization or amine modifications were purchased from Genscript (sense: 5'-AACATGTCTGGACCCTGCCCTCATATCACCTGCGTTTCCGTTAAACTATCGGTTGCGGCCATATCTACCAGAAAGCACCGTTTCCCGTCCGATCAACTGTAGTTAAGCTGGTAAGAGCCTGACCGAGTAGTGTAGTGGG/iAmMC6dT/GACCATACGCGAAACTCAGGTGCTGCAATCTGTAGATTCATTGGACTGGTG-3'; antisense: 5'-AGATTGCAGCACCTGAGTTTCGCGTATGGTCACCCACTACACTACTCGGTCAGGCTCTTACCAGCTTAACTACAGTTGATCGGACGGGAAACGGTGCTTTCTGGTAGATA/iAmMC6dT/GGCCGCAACCGATAGTTTAACGGAAACGCAGGTGATATGAGGGCAGGGTCCAGACATGTTACTGGGGAATTCCATGGTCCGTA-3';

sense, biotinylated: 5'-/5BiotinTEG/TACGGACCATGGAATTCCCCAGT-3').

Oligonucleotides, carrying an amine group, were labeled with NHS ester-conjugated fluorescent dyes. For the labeling reaction, 6.25 μl of 40 μM amine-modified antisense DNA was mixed with an excess of NHS ester-conjugated Cy3 dye (200:1 ratio of dye to DNA) in 100 mM Na2B4O7 pH8.4 and 40% DMSO. The mix was incubated at 25°C for 6 hours, then at 4°C overnight on a gently shaking mixer in the dark. The excess dye was removed by ethanol precipitation and 70% ethanol wash. The labeling reaction was performed twice to increase labeling efficiency. Amine-modified sense DNA was labeled with NHS ester-conjugated Cy5 dye in the same way. The dsDNA construct (1 μM) was prepared by mixing the biotinylated sense DNA with sense DNA-Cy5 and antisense DNA-Cy3 at a molar ratio of 1.2:1.1:1 and annealed in water in a heat block by incubation at 95°C for 5 minutes followed by gradual cooling to RT.

Complex assembly and pulldown for smFRET

To achieve consistency between the two methods, we performed the protein-DNA complex assembly in the same way as preparing the cryo-EM samples with a few modifications. The annealed and Cy3-/Cy5-labeled dsDNA construct was used instead of the 5S rRNA gene DNA template. After the complex elution with EcoRI, 1.2 pmol of antisense biotinylated DNA (5'-/5BiotinTEG/CACCAGTCCAATGAATCTAC-3') was added to the elution and incubated at RT for 10 minutes. The integrity of TFIIIA-TFIIIC and TFIIIA-TFIIIC-Brf1-TBP complexes assembled on fluorescently labeled DNA was confirmed by negative stain EM. The sample was incubated on ice before the smFRET experiment.

smFRET measurements

Single-molecule experiments were performed in a flow chamber prepared by sandwiching PEG (mPEG and biotin-PEG 1% (w/w), Laysan Bio) passivated glass coverslip (VWR) and slides (ThermoFisher Scientific).[91] Before imaging, flow chambers were washed with T-50 buffer (50 mM NaCl, 10 mM Tris, pH 7.4) and incubated with 50 nM NeutrAvidin (ThermoFisher Scientific) for 2 minutes. Then the flow chambers were washed with T-50 to remove unbound NeutrAvidin. Finally, the pre-assembled complex of labeled DNA and proteins, as described above, was injected into the chamber to immobilize on the surface. The complex was diluted and imaged in an imaging buffer consisting of 4 mM Trolox, 10 mM HEPES, 10 mM $MgCl_2$, 50 mM KCl, 5uM $ZnCl_2$, 5 % glycerol, and an oxygen-scavenging system consisting of 4 mM protocatechuic acid (Sigma) and 1.6 Uml^{-5} bacterial protocatechuate 3,4-di-oxygenase (rPCO) (Oriental Yeast), pH 7.35. All the chemicals were purchased from Sigma (purity >99.9%).

smFRET data were recorded at 50 ms time resolution using a TIRF microscope with a 100x oil-immersion objective (Olympus, NA 1.49). The donor and acceptor fluorophores were excited using 532 nm and 638 nm lasers, respectively.

smFRET data analysis

Single-molecule fluorescence intensity traces were analyzed using smCamera (http://ha.med.jhmi.edu/resources/), custom-written Matlab (MathWorks) scripts, and OriginPro. smFRET particles were selected based on the Gaussian intensity profile of the spots, acceptor brightness at least 5% above the background, and the acceptor signal upon donor excitation. The donor and acceptor intensity traces were selected based on the following criteria. A single donor and a single acceptor bleaching step during the acquisition time window, stable total intensity ($I_D + I_A$), and anticorrelated intensity profiles of donor and acceptor without blinking. Two authors independently examined all the data and found identical results. Each experiment, unless otherwise noted, was carried out three times to ensure that the findings could be repeated. Apparent FRET efficiency was calculated using ($I_A - efficienc_D$)/(I_D (fic_A), where I_D and I_A are raw donor and acceptor intensities, respectively. smFRET histograms for the DNA, DNA+TFIIIA+TFIIIC, and DNA+TFIIIA+TFIIIC+Brf1-TBP were generated from the 3, 4, and 16 movies from different days.

To determine the FRET value, the smFRET histograms were fitted using OriginPro with 1 or 2 Gaussian distributions.

$$y(x) = \sum_{i=1}^{n} \frac{A_i}{w_i \sqrt{\frac{\pi}{2}}} e^{-2\frac{(x-xc_i)^2}{w_i^2}}$$

where n is the number of Gaussians, A is the peak area, xc is the FRET peak center, and w is the full-width half maximum for each peak.

To derive the transition density plots (TDPs), all the time traces were idealized by fitting with hidden Markov model (HMM) using vbFRET software in Matlab.[92] Traces were fit with 1 to 4 step models and majority of traces fit with a 1 or 2 steps. Then, from the idealized traces, all the transitions were extracted to create a transition density plot.

QUANTIFICATION AND STATISTICAL ANALYSIS

All the single molecule traces were acquired and analyzed using customized MATLAB codes.

smFRET histograms were generated by aggregating multiple movies acquired from at least two independent measurements. Error bars represent the standard error of the mean (SEM).